nanomaterials

Review

Strain Engineering of Intrinsic Ferromagnetism in 2D van der Waals Materials

Hongtao Ren [1,*] and **Gang Xiang** [2,*]

[1] School of Materials Science and Engineering, Liaocheng University, Hunan Road No. 1, Liaocheng 252000, China
[2] College of Physics, Sichuan University, Wangjiang Road No. 29, Chengdu 610064, China
* Correspondence: renhongtao@lcu.edu.cn (H.R.); gxiang@scu.edu.cn (G.X.)

Abstract: Since the discovery of the low-temperature, long-range ferromagnetic order in monolayers $Cr_2Ge_2Te_6$ and CrI_3, many efforts have been made to achieve a room temperature (RT) ferromagnet. The outstanding deformation ability of two-dimensional (2D) materials provides an exciting way to mediate their intrinsic ferromagnetism (FM) with strain engineering. Here, we summarize the recent progress of strain engineering of intrinsic FM in 2D van der Waals materials. First, we introduce how to explain the strain-mediated intrinsic FM on Cr-based and Fe-based 2D van der Waals materials through ab initio Density functional theory (DFT), and how to calculate magnetic anisotropy energy (MAE) and Curie temperature (T_C) from the interlayer exchange coupling J. Subsequently, we focus on numerous attempts to apply strain to 2D materials in experiments, including wrinkle-induced strain, flexible substrate bending or stretching, lattice mismatch, electrostatic force and field-cooling. Last, we emphasize that this field is still in early stages, and there are many challenges that need to be overcome. More importantly, strengthening the guideline of strain-mediated FM in 2D van der Waals materials will promote the development of spintronics and straintronics.

Keywords: strain engineering; ferromagnetism; transition metal trihalides; transition metal chalcogenides; transition metal phosphorous chalcogenides; wrinkle; flexible substrates; lattice mismatch; spintronics; straintronics

check for updates

Citation: Ren, H.; Xiang, G. Strain Engineering of Intrinsic Ferromagnetism in 2D van der Waals Materials. *Nanomaterials* **2023**, *13*, 2378. https://doi.org/10.3390/nano13162378

Academic Editor: Stefano Agnoli

Received: 9 July 2023
Revised: 9 August 2023
Accepted: 17 August 2023
Published: 19 August 2023

Copyright: © 2023 by the authors. Licensee MDPI, Basel, Switzerland. This article is an open access article distributed under the terms and conditions of the Creative Commons Attribution (CC BY) license (https://creativecommons.org/licenses/by/4.0/).

1. Introduction

According to the *Mermin–Wanger–Hohenberg* theory [1,2], thermal fluctuations can destroy the long-range magnetic order of 2D systems at finite temperatures. However, the anisotropy of the system suppresses thermal disturbances by opening the gap in the spin-wave spectrum [3–6]. Furthermore, spin orbit coupling (SOC) can stabilize the long-range magnetic order in 2D systems by contributing to magnetic anisotropy. After the discovery of the low-temperature, long-range ferromagnetic order in monolayers $Cr_2Ge_2Te_6$ and CrI_3 [7,8], many efforts have been made to achieve a room temperature (RT) ferromagnet. Indeed, strain engineering [9–25] is a very important strategy for mediating material properties, including optoelectronic [9,10,13–15,21], electrocatalytic [11,16,22–24], and magnetic properties [15,19,21,24–28]. Since Novoselov et al. [29] obtained a stable monolayer graphene in the laboratory in 2004, further research gradually revealed that 2D materials, such as MoS_2, could withstand up to 20% strain [30–33]. However, it was very difficult to directly apply strain to 2D materials in experiments, which made strain-controlled performance largely remain in theoretical study. This was because by changing lattice parameters, strain could be easily applied to the lattice of 2D materials. Specifically, the study on strain-mediated magnetism in 2D materials, especially in 2D van der Waals materials with intrinsic long-range FM order, was focused on theoretical calculation. More interestingly, the $Bi_2Te_3 | Fe_3GeTe_2$ heterostructure related to strain [34,35] was designed to increase the Curie temperature (T_C) due to the proximity effect [36–40].

Very recently, some significant progress was also made in the field of experimental research [27,28,41–48]. In Figure 1, we summarize the recent progress of strain engineering of intrinsic ferromagnetism (FM) in 2D van der Waals materials. First, we introduce how to explain the strain-mediated intrinsic FM on Cr-based and Fe-based 2D van der Waals materials with long-range FM order through ab initio Density functional theory (DFT), and how to calculate magnetic anisotropy energy (MAE) and Curie temperature from the interlayer exchange coupling J. Subsequently, we focus on numerous attempts to apply strain to 2D materials in experiments, including wrinkle-induced strain, flexible substrate bending or stretching, lattice mismatch, electrostatic force and field-cooling. Last, we emphasize that this field is still in early stages, and there are many challenges that must be overcome. More importantly, strengthening the guideline of strain-mediated FM in 2D van der Waals materials will promote the development of spintronics [6,49–57] and straintronics [12,19]. As shown in Figure 1, we summarize three different kinds of 2D materials with intrinsic long-range FM order, including transition metal trihalides ($CrCl_3$, $CrBr_3$ and CrI_3) [5,58–72], transition metals chalcogenides ($Cr_2Ge_2Te_6$, Fe_nGeTe_2 and $CrTe_2$) [42–46,73–87], and transition metal phosphorous chalcogenides ($AgVP_2Se_6$, $CrPS_4$) [88–91].

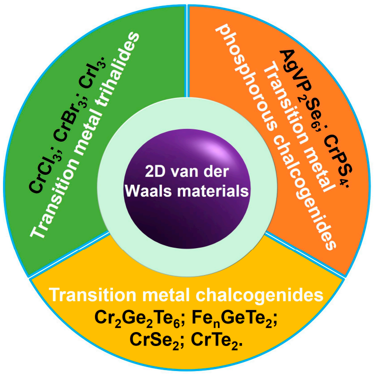

Figure 1. The three different kinds of 2D van der Waals materials with intrinsic long-range FM order.

2. Theoretical Calculations

In order to understand the essence of 2D ferromagnetism, ab initio Density functional theory, including linear density approach (LDA) [59], local spin density approximation (LSDA) [92], the generalized gradient approach (GGA) [61,93,94], and DFT + U [95,96], was often used to calculate the electronic structure of the system as a starting point. Moreover, the interlayer exchange coupling J was closely related to magnetic anisotropy, and it would also be used to calculate T_C [86,97–100]. The mean field theory [97,101] would roughly estimate T_C but, often, T_C overestimated it. Although the random phase approximation (RPA) could more accurately estimate T_C of three-dimensional (3D) materials, it may fail in 2D systems with large anisotropy. Notably, classic Monte Carlo (MC) [6,97] simulations can also describe the critical temperature.

2.1. Cr-Based 2D van der Waals Materials

2.1.1. $CrCl_3$

Unlike bulk materials, 2D materials can sustain larger strains [33,102]. Similarly, single-layer transition metal trihalides (MX_3, I, Cl and Br) can also withstand a strain of about 10% [58]. As a typical example, Yan et al. [59] studied the biaxial strain dependence magnetic anisotropy energy (MAE) of the 2D monolayer $CrCl_3$ (Figure 2a–d). When the compressive strain reached 2.5%, a phase transition from antiferromagnetism (AFM) to FM occurred (Figure 2e). In addition, when tensile strain was 2.4%, the maximum Curie temperature (T_C) reached 39 K. The MAE in the unstrained monolayer was positive, indicating the spins of Cr atoms were off-plane (Figure 2f).

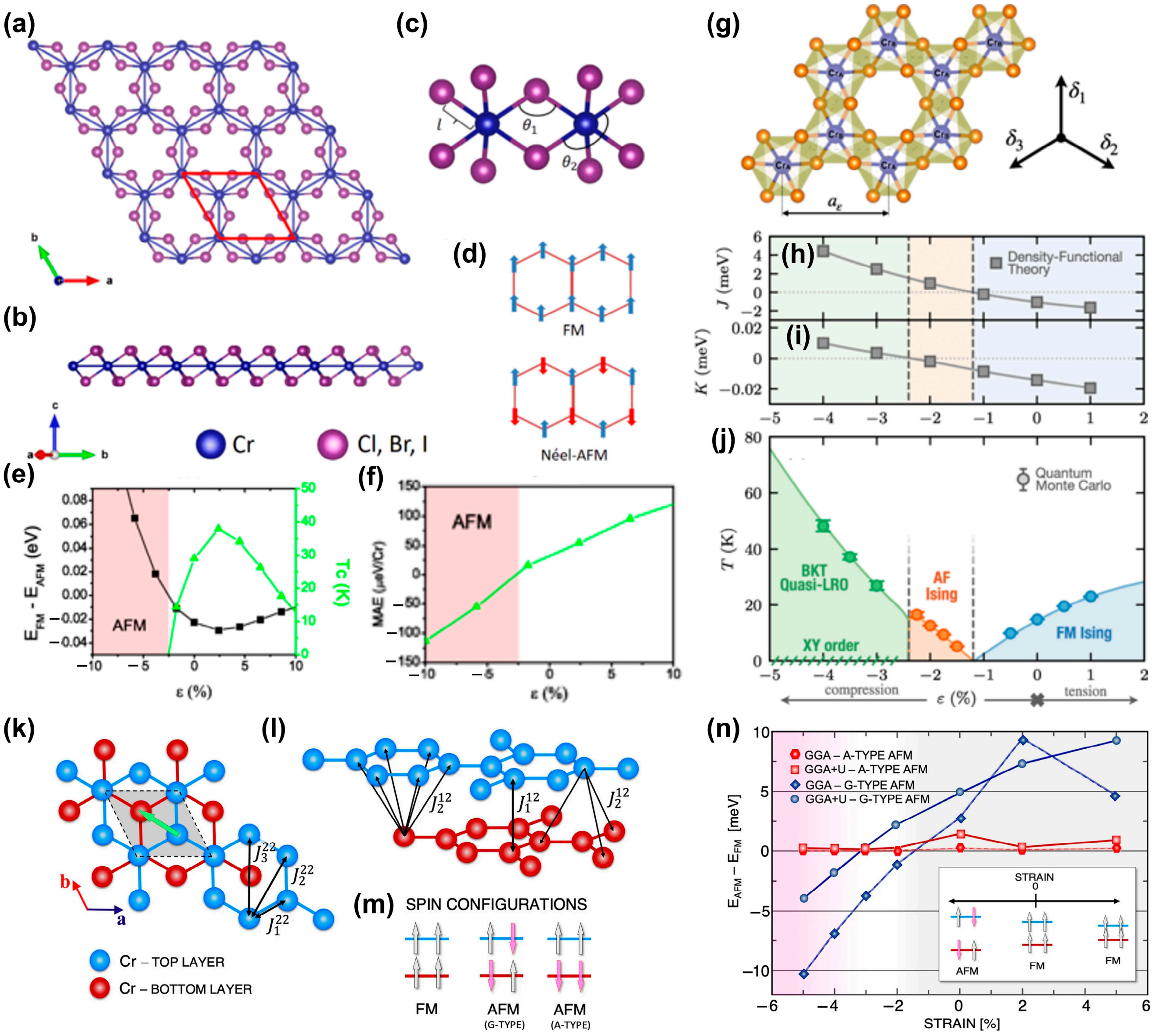

Figure 2. (**a**) Top and (**b**) side view of atomic structure of monolayer CrX_3 (X = Cl, Br, I). (**c**) Bonding between chromium and iodine atoms. The unit cell of CrX_3, which includes two Cr and six X atoms, has been indicated in (**a**). The bond length between Cr and an X atom, the bond angle θ_1 between Cr and two X atoms in the same plane, and the axial angle θ_2 are also shown in (**c**). (**d**) The two magnetic orders, namely AFM and FM. Energy difference between the FM and AFM phases for (**e**) $CrCl_3$. The AFM phase region is highlighted in red. The calculated T_C is also shown for each case. Change in MAE with respect to strain in (**f**) $CrCl_3$. (Reproduced with permission from [59]. Copyright 2016, American Physical Society). (**g**) Crystal structure of monolayer $CrCl_3$. Dashed lines denote the unit cell with basic vectors $\delta_1 = a_\varepsilon(0,1), \delta_2 = a_\varepsilon\left(\sqrt{3}/2,\ -1/2\right), \delta_3 = a_\varepsilon\left(-\sqrt{3}/2, -1/2\right)$, with strain-dependent lattice constanta a_ε. (**h**,**i**) Magnetic nearest-neighbor superexchange J and anisotropy K of Hamiltonian (1), respectively, computed via Density Functional Theory (DFT) as a function of monolayer strain ε. (**j**) Finite−temperature phase diagram of the monolayer $CrCl_3$ versus strain ε. Strain drives the monolayer into three different finite−temperature magnetic phases: BKT quasi-LRO phase, AFM Ising, and FM Ising. (Reproduced with permission from [63]. Copyright 2021, American Physical Society). (**k**,**l**) Arrangement of Cr atoms in the lattice of the $CrCl_3$ bilayer in the low temperature phase. The green arrow indicates the direction of lateral shift between the top and bottom layers. (**m**) Schematic plot of three different spin configurations of bilayer $CrCl_3$. (**n**) The energy difference between the FM and AFM phases. (Reproduced with permission from [64]. Copyright 2023, Springer Nature).

After applying the strain to the lattice, Cl atoms adjusted their position to minimize the lattice distortion energy at this strain (Figure 2g). After generating a specific structure, the energy difference between the ferromagnetic and antiferromagnetic states was calculated. Mapping this energy difference to the Hamiltonian (1), Dupont et al. [63] obtained the nearest-neighbor exchange coupling J and magnetic anisotropy K, as shown in Figure 2h,i.

$$\hat{H} = J_{\varepsilon} \sum_{\langle \vec{r}, \vec{r}' \rangle} \hat{\vec{S}}_{\vec{r}} \cdot \hat{\vec{S}}_{\vec{r}'} + K_{\varepsilon} \sum_{\vec{r}} \left(\hat{\vec{S}}^{z}_{\vec{r}} \right)^{2} \tag{1}$$

Note that: the spin value of S was $3/2$ in the above equation.

As the strain evolved from compression to tension, the system sequentially exhibited the BKT (Berezinskii–Kosterlitz–Thouless) quasi-long-range order (LRO) phase, AFM Ising and FM Ising by QMC (Quantum Monte Carlo) simulations. Although theoretical and experimental studies have been conducted on monolayer and bulk $CrCl_3$ materials, research on their multilayer structures, including bilayers and trilayers systems, was very limited. Ebrahimian et al. [64] found that biaxial strains could also achieve a phase transition from AFM to FM (Figure 2k–n). In addition, the magnetic anisotropy could be mediated by the strain.

2.1.2. $CrBr_3$

More interestingly, the Curie temperature of monolayer $CrBr_3$ could be increased to 314 K by doping [103], which was between $CrCl_3$ (323 K) and CrI_3 (293 K). Although both hole doping and electron doping could enhance ferromagnetic coupling, the effect of hole doping was better at the same doping concentration. After applying biaxial strain to a unit cell, its magnetic moment remained unchanged, which indicated that the biaxial strain could not effectively enhance the ferromagnetic coupling of monolayer CrX_3. In addition, Webster et al. [59] found that applying a tensile strain of 2.1% could increase the T_C to 44 K, which was about 5 K higher than when no strain was applied. However, at a compressive strain of −4.1%, a FM to AFM phase transition, similar to $CrCl_3$ [59,63,64] and CrI_3 [59,70–72], also occurred.

2.1.3. CrI_3

Unlike monolayer $CrCl_3$, the electronic bandgap of monolayer CrI_3 remained almost unchanged after applying biaxial tensile strain; after applying biaxial compressive strain, the electronic bandgap decreased significantly and MAE increased significantly. When compressive strain reached 5%, MAE increased by 47% [59]. Continuing to increase the strain (−5.7%) resulted in a phase transition from FM to AFM. Similar to $CrCl_3$, Wu et al. [69] also found that the CrI_3 monolayer underwent a complex phase transition from magnetic metals, half-metal, half-semiconductor to magnetic semiconductor as the strain evolved from compression (−15%) to tension (10%).

As a typical example, Vishkayi et al. [71] investigated the effects of biaxial and uniaxial strain on the magnetism of monolayer CrI_3 (Figure 3a–e). A similar phase transition from FM to AFM [59] was also observed when a compressive strain greater than 7% was applied (Figure 3d). As the strain increased, the electronic bandgap showed an opposite trend when applying compressive or tensile strain (Figure 3d). Interestingly, uniaxial strain enhanced the nearest neighbor, Dzialoshinskii–Moriya (DM) interaction, by breaking the inversion symmetry, and its effect was stronger than biaxial strain.

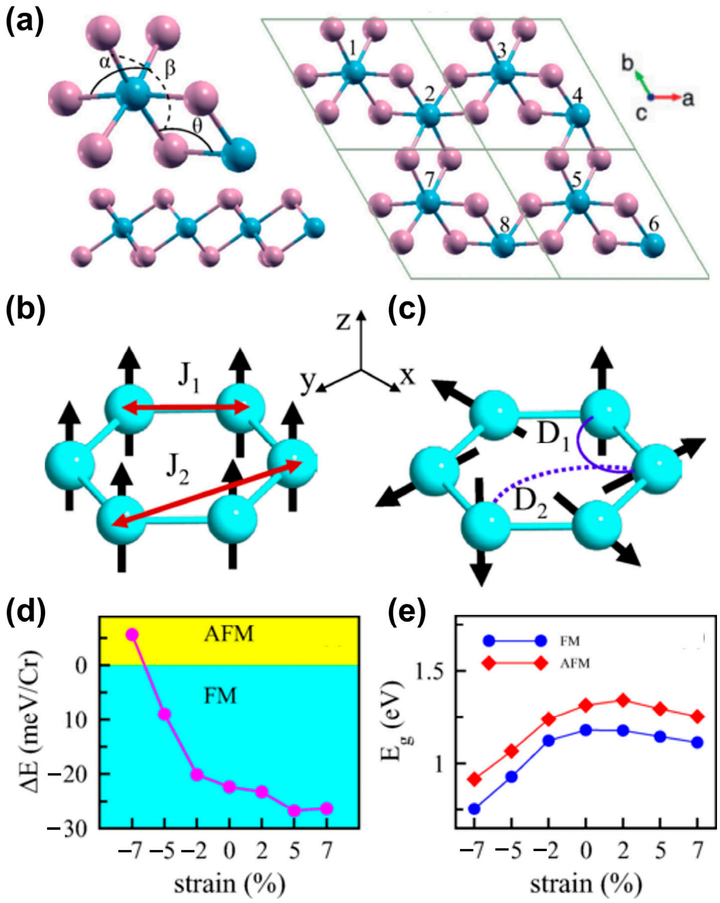

Figure 3. (**a**) Top and side views of monolayer CrI_3. The bonding angles between the atoms in the monolayer are denoted by θ, α, and β. A 2 × 2 × 1 supercell of the monolayer. The blue (pink) spheres represent Cr(I) atoms. (**b**) Schematic picture of the symmetric exchange couplings between Cr atoms, where J_1 denotes the coupling between nearest-neighbor atoms and J_2 denotes the coupling between next-nearest-neighbor atoms. (**c**) The same as (**b**) for the DM vectors. (**d**) The total energy difference between the FM and AFM configurations, ΔE, and (**e**) the variation in the band gap as a function of strain for monolayer CrI_3 in the FM and AFM configurations. (Reproduced with permission from [71]. Copyright 2020, American Physical Society).

The phase transition from FM to AFM under compressive strain (−3% or −5%) had also been discovered in the CrI_3 bilayer [70], similar to other previously reported systems [59,71]. In addition, Safi et al. [72] found that the phase transition occurred at −6% compressive strain. More importantly, they also discovered a second phase transition point from FM to AFM, which occurred near −2.5% compressive strain.

2.1.4. $CrTe_2$

Guo et al. [104]. found that applying uniaxial or biaxial tensile strain to monolayer $CrTe_2$ in the *T* phase did not cause a phase transition from direct to indirect bandgap. Under biaxial strain, the $CrTe_2$ monolayer [105] underwent phase transformation at −1% compressive strain in Figure 4a–k.

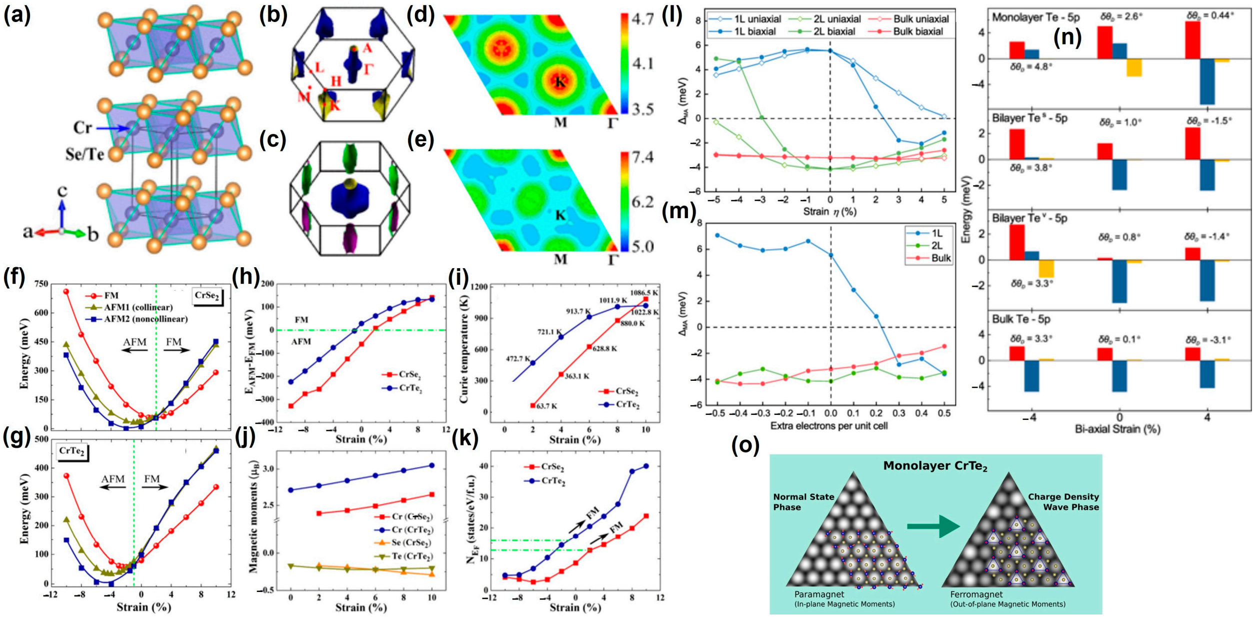

Figure 4. (**a**) Crystal structure of $CrSe_2/CrTe_2$ bulk; Fermi surface without spin polarization for (**b**) $CrSe_2$ and (**c**) $CrTe_2$ bulks; real part of electron susceptibility χ' with $q_z = 0$ for (**d**) $CrSe_2$ and (**e**) $CrTe_2$ bulks. Relative total energies of three different magnetic configurations [FM, AFM1 (collinear), and AFM2 (non-collinear)] as a function of biaxial strain for (**f**) $CrSe_2$ and (**g**) $CrTe_2$ monolayers. Strain dependence of (**h**) the energy difference ΔE ($=E_{AFM} - E_{FM}$) between AFM and FM states in one unit cell, (**i**) the T_C in FM states, (**j**) magnetic moments on Cr and Se/Te atoms in FM states, and (**k**) the number of density of states (DOS) at the Fermi energy N_{EF} in the nonmagnetic (NM) states for $CrSe_2/CrTe_2$ monolayers. (Reproduced with permission from [105]. Copyright 2015, American Physical Society). (**l**) strain and (**m**) band filling of 1 L, 2 L, and bulk 1T-$CrTe_2$. Difference in SOC matrix elements $\Delta_{<pi|pj>}$ (per atom) of the Te-5p orbitals. (**n**) $\Delta_{<pi|pj>}$ of 1 L, 2 L, and bulk 1T-$CrTe_2$ versus strain. At each strain, the values for $\delta\theta_D$ are also shown. Positive and negative values of the strain correspond to tensile and compressive strain, respectively. For the bilayer, values for Te atoms at the van der Waals gap (Te^v) and Te atoms at the free surface Te^s are shown. (Reproduced with permission from [106]. Copyright 2022, American Physical Society). (**o**) Computed STM images for monolayer $CrTe_2$ in the normal state and the charge density wave (CDW) phase. (Reproduced with permission from [107]. Copyright 2020, American Chemical Society).

Interestingly, the $CrTe_2$ monolayer with strain-free was a FM state. After the tensile strain was applied, its T_C could rise to 1022.8 K [106], and the magnetic moment of Cr atom increased linearly, which may be caused by the increase of the density of states at Fermi energy N_{EF}. Magnetic anisotropy exhibited a different sensitivity to uniaxial and biaxial strain, as shown in Figure 4l. A monolayer was more sensitive to tensile strain, while a bilayer was more sensitive to compressive strain, and bulk was insensitive to the applied strain. Furthermore, band filling [108] of the monolayer also underwent a transition from out-of-plane to in-plane, while the bilayer and bulk did not undergo this transition (Figure 4m). More interestingly, the strain had the greatest impact on the dihedral angle θ_D, followed by the effect of Cr-Te-Cr bond length (Figure 4n). Notably, the charge density wave (CDW) phase [107] promoted greater stability of the long-range FM order.

2.1.5. $Cr_2Ge_2Te_6$

As early as 2014, Li et al. [73] predicted that $Cr_2X_2Te_6$ (X = Si, Ge), a layered crystal with intrinsic FM, could be obtained experimentally by exfoliation. Furthermore, the T_C of $Cr_2Ge_2Te_6$ ($Cr_2Si_2Te_6$) was increased by 51.7(56) K under an isotropic tensile strain. Similarly, Dong et al. [75] also found that $Cr_2Ge_2Se_6$ and $Cr_2Ge_2Te_6$ were a stable FM semiconductor, as shown in Figure 5a–e.

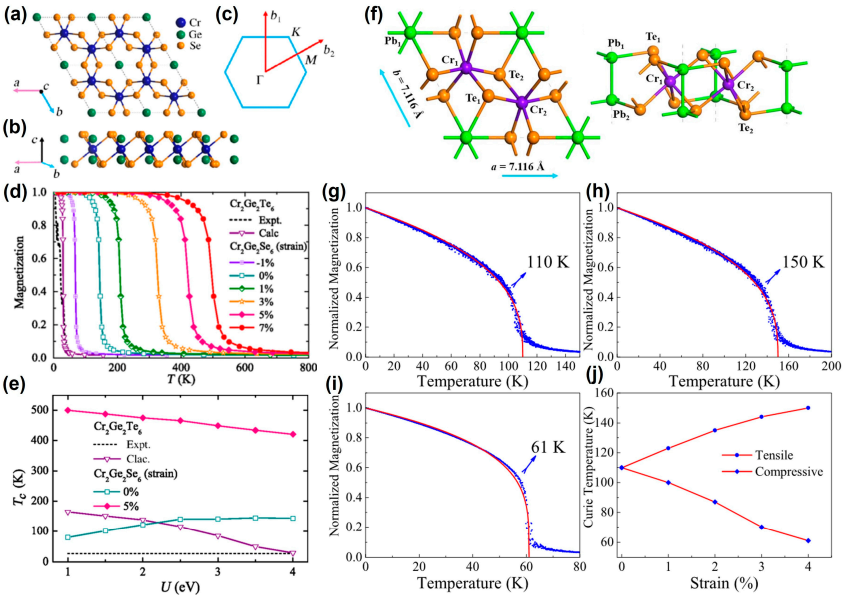

Figure 5. (**a**) top view in the *a*-*b* plane and (**b**) side view in the *a*-*c* plane of crystal structure of $Cr_2Ge_2Se_6$. The 2D Brillouin zone is shown in (**c**). (**d**) *M*-*T*. The experimental results for are taken from Ref. [7]. The calculated results are obtained by DFT calculations and Monte Carlo simulations. (**e**) T_C-U. (Reproduced with permission from [75]. Copyright 2019, American Physical Society). (**f**) top and side view of crystal structure of $CrPbTe_3$. *M*-*T* curves for (**g**) pristine $CrPbTe_3$, (**h**) 4% tensile strain structure, (**i**) 4% compressive strain structure and (**j**) variation of T_C with strain. (Reproduced with permission from [78]. Copyright 2020, IOP Publishing).

Through Monte Carlo simulation, it was found that the T_C of $Cr_2Ge_2Se_6$ (144 K) was five times that of $Cr_2Ge_2Te_6$ (30 K) (Figure 5d). Interestingly, when compressive strain was applied, the T_C decreased, and even at 2% strain, the phase became AFM. After applying tensile strain, the T_C would be increased, even up to 500 K. Notably, the T_C of $Cr_2Ge_2Se_6$ with 5% strain was always higher than RT (Figure 5e). To our knowledge, 2D $Cr_2Ge_2Se_6$ has not yet been prepared experimentally.

As a member of Cr-based materials, 2D $CrPbTe_3$ (CPT) has a stable monolayer structure and a higher T_C, as shown in Figure 5f. Similar to $Cr_2Ge_2Se_6$, its T_C (110 K) gradually increased from compressive strain (61 K) to tensile strain (150 K) (Figure 5g–j). In addition, strain can also induce spin reorientation from the in-plane to the out-of-plane.

2.1.6. $CrPS_4$

$AgVP_2Se_6$, as a typical quaternary FM semiconductor, was synthesized by heating the elements in evacuated silica tubes as early as 1988 [88]. Ouvrard et al. found that its polycrystalline powder showed low-temperature FM, high-temperature PM and T_C of about 29 K. Recently, single crystal $AgVP_2Se_6$ samples [90] exhibited better stability than MX_3 materials. As another typical example, single crystal $CrPS_4$ [91] was obtained by the chemical vapor transport method and mechanical exfoliation. Interestingly, odd layers were ferromagnetic at lower temperatures, while even layers were antiferromagnetic, as shown in Figure 6. To the best our knowledge, there were currently no reports on regulating the magnetic properties of $AgVP_2Se_6$ and $CrPS_4$ through strain engineering.

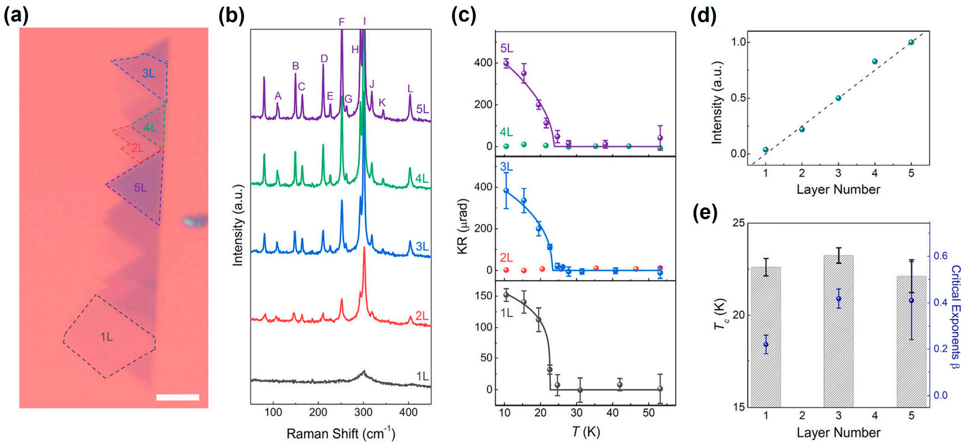

Figure 6. Layer dependent magnetic properties of thin $CrPS_4$. (**a**) Optical image. Scale bar is 5 μm. (**b**) Raman spectra. (**c**) Temperature dependence of MOKE signal under $\mu_0H = 0.25$ T measured on 1 L to 5 L flakes shown in (**a**). (**d**) Raman peak intensity of the F peak for each flake normalized by that from the 5 L as a function of the layer number. (**e**) Critical temperature, T_C (black dashed bar), and critical exponent, β (blue symbol), extracted from the fitting lines shown in (**c**). (Reproduced with permission from [68]. Copyright 2021, American Chemical Society).

2.2. Fe-Based 2D van der Waals Materials

The bulk Fe_3GeTe_2 (FGT) with the hexagonal platelets was first synthesized by a direct solid-state reaction (SSR) [81]. Zhuang et al. [82] found that applying biaxial strain on single-layer metallic Fe_3GeTe_2 could enhance the MAE and total magnetic moment (Figure 7a–d). When 2% tensile strain was applied, its MAE increased by 50%; After the applied strain changed from compression to tension, the total magnetic moment also increased with the increase of strain. Through DFT calculations, Hu et al. [85] discovered that monolayer FGT was a metallic type ferromagnet, with its magnetic moment mainly localized on Fe atoms and its metallicity mainly derived from the Fe *d* orbitals in Figure 7e–g.

After applying the biaxial strain shown in Figure 7h, there was a significant change in the spin-density distributions of the FGT monolayer. The magnetism of this system mainly came from Fe atoms (Figure 7i), especially Fe3 atoms at the inequivalent site (Figure 7f), with little contribution from Ge and Te atoms (Figure 7j). Due to the Poisson effect, when stretched in the in-plane direction, it contracted in the out of plane direction. Therefore, as the bond lengths of Fe1-Te and Fe3-Te were reduced in the plane, the bond lengths of Fe3-Te in the vertical direction were increased (Figure 7k). Biaxial strain caused a change in bond length, thereby promoting charge transfer within the monolayer (Figure 7l). When the biaxial strain increased from −5% to 5%, the spin splitting of the Fe1 3d orbital near the Fermi level became larger, as shown in Figure 7m; after the strain was applied, the spin polarization of Fe3 atoms would increase in Figure 7n, which would cause the magnetic moment to increase. In conclusion, biaxial strain-mediated FM in the FGT monolayer was closely related to the charge transfer between Fe1 and Te atoms.

Previous studies have mainly focused on biaxial strain-mediated FM in the FGT monolayers [82,85], without studying the modulation mechanism of uniaxial strain on FM. As a typical example, Zhu et el. [86] investigated the uniaxial (ε_a and ε_c) and isotropic ($\varepsilon_{iso.}$) strain modulation of the exchange coupling constant J_{ij} and T_C in FGT. As shown in Figure 8, three different magnetic configurations (FM, AFM1, and AFM2) were considered. The total energy of AFM2 was much higher than those of FM and AFM1.

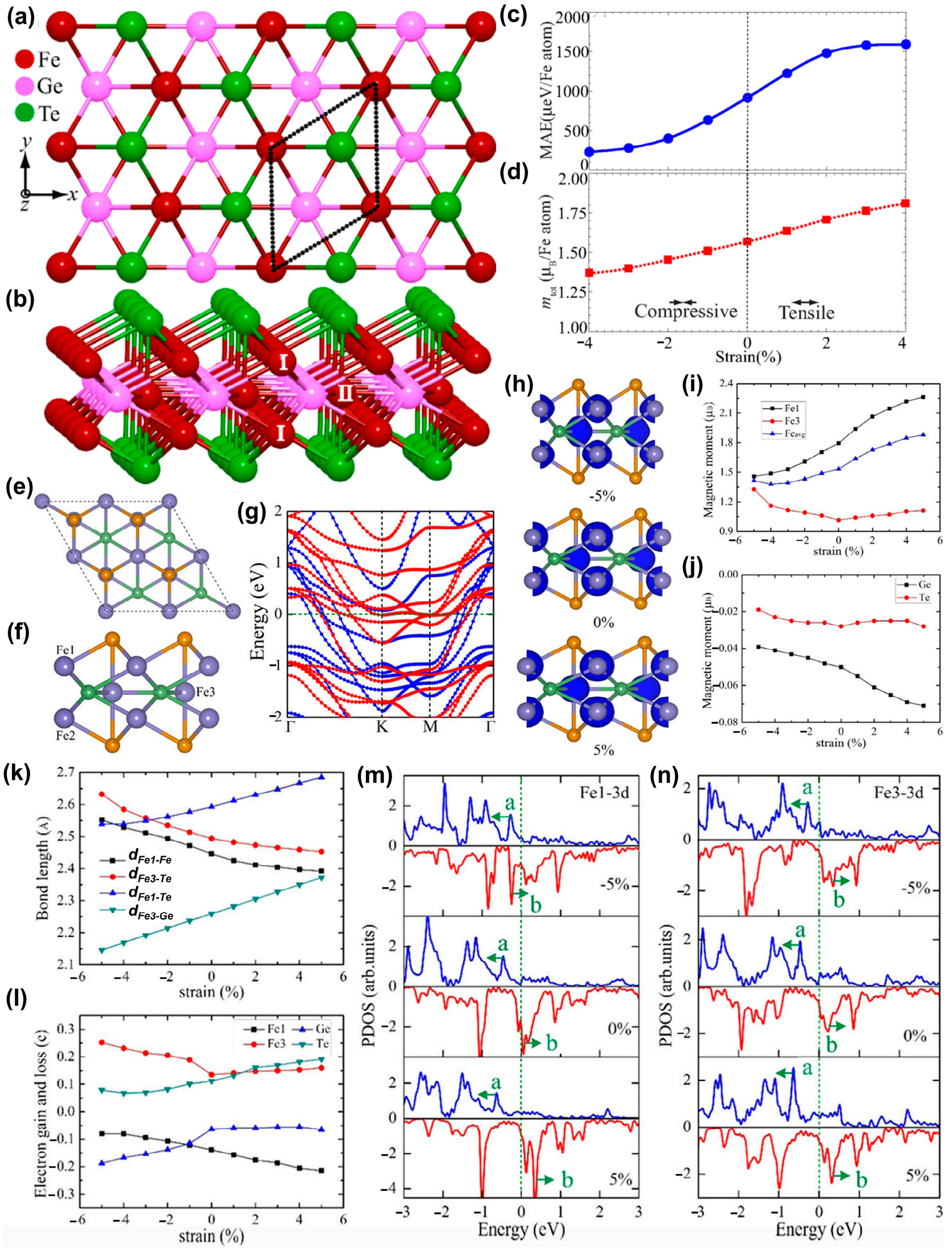

Figure 7. (**a**) Top and (**b**) side views of the atomic structure of monolayer Fe_3GeTe_2. The unit cell is enclosed by the dotted lines. Inequivalent Fe sites are numbered by I and II, respectively. Variation of (**c**) MAE and (**d**) total magnetic moment per Fe atom of single-layer Fe_3GeTe_2 under biaxial strain. (Reproduced with permission from [82]. Copyright 2016, American Physical Society). (**e**) Top and (**f**) side views of the structural models of the FGT monolayer. The purple, green, and yellow balls stand for Fe, Ge, and Te atoms, respectively. Fe sites are numbered by Fe1, Fe2, and Fe3, respectively, where Fe1 and Fe2 atoms are located at 2 equivsites, while Fe3 atom has the inequivalent site. (**g**) Spin-polarized band structures of the FGT monolayer. The Fermi level is set at zero, denoted by the olive dashed line. (**h**) Spin-density distribution of the FGT monolayer with −5, 0, and 5% strain. The isovalues are 0.02 e/Å^3. Strain dependence of magnetic moment (**i**) per Fe1 and Fe3 atoms and (**j**) per Ge and Te atoms in the FGT monolayer. Strain dependence of (**k**) the distance and the bonding length (Fe1–Fe2 distance, $d_{Fe1\text{-}Fe2}$; Fe3–Te bond length, $d_{Fe3\text{-}Te}$; Fe1−Te bond length, $d_{Fe1\text{-}Te}$; Fe3–Ge bond length, $d_{Fe3\text{-}Ge}$). (**l**) Electron transfer of Fe, Ge, and Te atoms in the FGT monolayer. PDOS (partial density of states) of (**m**) Fe1 atom and (**n**) Fe3 atom in the FGT monolayer. The enhanced spin splitting of the a and b states in PDOS. (Reproduced with permission from [85]. Copyright 2020, American Chemical Society).

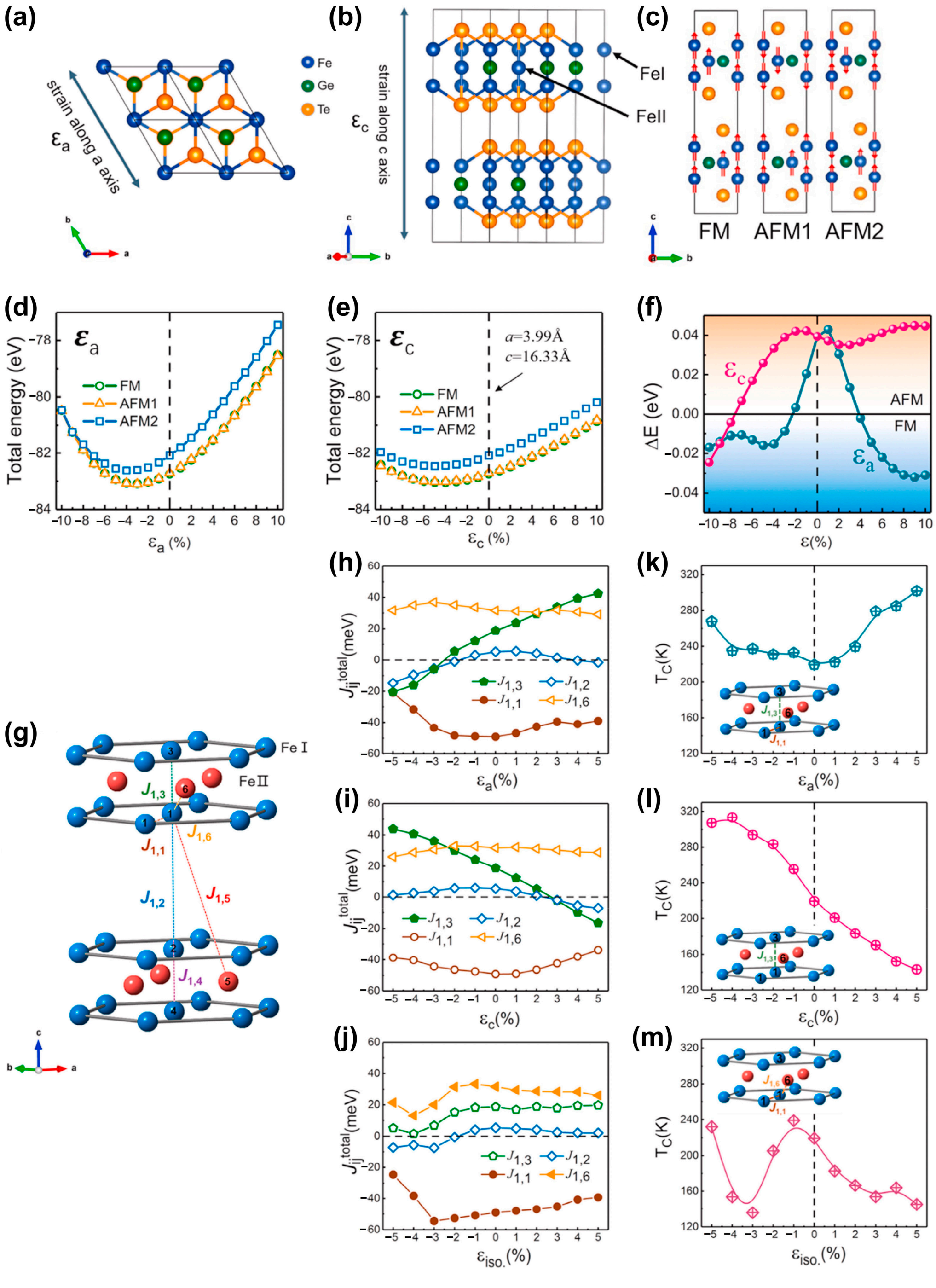

Figure 8. Schematic of the crystal structure of FGT from (**a**) top and (**b**) side view, and (**c**) the spin structure of FM, AFM1, and AFM2 configurations. (**d**,**e**) Total energy of FM, AFM1, and AFM2 configurations of FGT as a function of lattice distortion (**d**) along the a-axis and (**e**) the c-axis. (**f**) Total energy difference ($\Delta E = E_{FM} - E_{AFM}$) under c-axis and a-axis strain. The background indicates the FM- or AFM-stable region. (**g**) The schematic picture of Fe–Fe exchange interactions in FGT, where only the Fe atoms are displayed. (**h**–**j**) Total isotropic exchange coupling parameters of $J_{1,1}$, $J_{1,2}$, $J_{1,3}$, $J_{1,6}$ in functions of three different kinds of distortion: (**h**) along the a-axis, (**i**) along the c-axis and (**j**) isotropically. (**k**–**m**) Corresponding variation of T_C under above strains. The insets show the $J_{i,j}$ that play a main role in the variation of T_C. (Reproduced with permission from [86]. Copyright 2018, Elsevier).

The system exhibited a phase transition from AFM to FM, similar to the modulation result of biaxial strain [59]. Interestingly, when the strain (ε_a) along the a-axis was applied, the phase transition occurred at a tensile of ~4% or compressive of ~2%; when the strain (ε_c) along the c-axis strain was applied, it occurred at a compressive of ~8–10%. Furthermore, the strain-mediated variation of $J_{ij}{}^{total}$ is shown in Figure 8g–i. T_C could be estimated by the following equation [86,98,99]:

$$T_C = \frac{2}{3K_B} J_{max} \tag{2}$$

Note that J_{max} is the maximal eigenvalue of the matrix consisting of the exchange coupling between different atoms [86,109]. After applying the uniaxial strain, the T_C could be raised to room temperature (Figure 8k–m). When isotropic strain is applied, the T_C exhibited complex nonlinear changes and failed to reach room temperature (Figure 8m). Their results demonstrated that applying uniaxial strain was an effective way to elevate the T_C.

Regarding another interesting compound, Fe_5GeTe_2 [110,111], recent experiments have found that it has a higher T_C. However, little is known about the electronic and magnetic properties of its monolayer. Joe et al. [83] found that the magnetism of bulk and monolayer metallic Fe_5GeTe_2 originated from Fe d orbital. Moreover, biaxial strain could also enhance the Fe magnetic moment from 1.65 μ_B to 2.66 μ_B.

3. Introducing Strain in 2D van der Waals Materials

3.1. Wrinkle-Induced Strain

The previously discovered strain-mediated FM phenomena were all in 2D materials without intrinsic long-range magnetic order [27,28,41]. Very recently, Seidel et al. [42] found a clear dependence of T_C on the strain state and the thickness of $Cr_2Ge_2T_6$ (CGT). The layered CGT lattice with intrinsic magnetism was shown in Figure 9a. A stripe domain structure was observed with MFM (Figure 9b). After buckling, the wrinkled area had a higher T_C than the flat area on (Figure 9c). DFT calculations indicated that the strain could elevate the T_C in monolayer and bilayer $Cr_2Ge_2T_6$ (Figure 9d–g). In addition, the strain of three different wrinkles in Figure 9h was confirmed by COMSOL simulations. To the best of our knowledge, this was the first time that the strain distribution in CGT wrinkles was mapped with the COMSOL simulation. Furthermore, the magnetic signals could be observed at the wrinkled regions at RT through MFM.

3.2. Bending or Pre-Stretching Flexible Substrates

Similar to pre-stretched flexible substrates, including Gel-Film [30], polydimethylsiloxane (PDMS) [30,112–117], polyethyleneterephthalate (PET) [118], polyimide (PI) [47,119,120], and polyvinyl alcohol (PVA) [121,122], strain can also be introduced into 2D materials by bending flexible substrates. As a typical example, Yan et al. [121] designed a novel polymer-buried strategy to apply tensile strain on Fe_3GeTe_2 (FGT) nanoflakes (Figure 10a). Firstly, PVA was spin-coated onto pre-stretched mechanical exfoliated FTG nanosheets. Then, the PET sheet was attached to the surface of the PVA film and peeled off with tweezers. The complex film (FGT/PVA/PET) was placed into a non-magnetic plastic tube and then the tensile strain was applied on the FGT nanosheets through a three-point fixing device. As the applied strain gradually increased, the sample transitioned from its original PM state to FM states, as shown in Figure 10b,c. When the strain reached 4.7%, the hysteresis loop evolved from soft magnet to hard magnet; however, when the strain reached 7.0%, the hysteresis loop displayed an opposite evolution trend. Moreover, the M_s and H_c were very close to those found for the case of tensile strain. Unlike zero-strain samples, the sample with a 3.4% tensile strain always exhibited centrosymmetry and no exchange bias (Figure 10d,e). The hidden AFM state and interface–exchange interaction could be revealed by controlling the strain. The frequency shift was inverted after relaxing the strain, indicating the transition from FM state to PM state (Figure 10f,g). As the strain increased, the T_C was elevated above RT in Figure 10h,i. In short, strain engineering is an efficient way to increase T_C compared to other methods (Figure 10j).

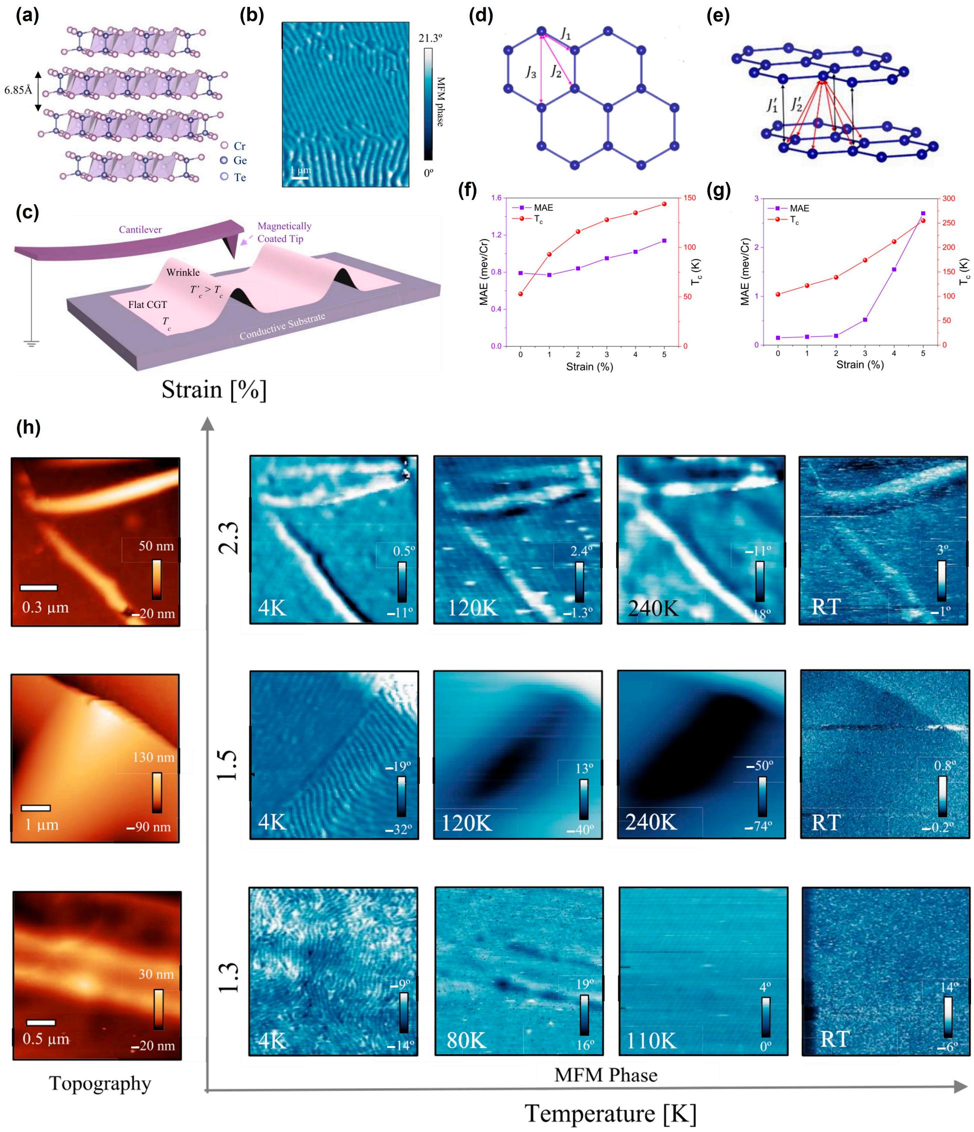

Figure 9. Curved nanostructures in *vdW* $Cr_2Ge_2T_6$: (**a**) CGT crystal lattice showing the *vdW* layered structure and interlayer distance. (**b**) Typical magnetic stripe domain structure at 4 K seen in MFM measurements. (**c**) Schematic showing wrinkles in layered CGT and magnetically coated tip for MFM measurements. DFT predicted trend of magnetism and transition temperature with strain percentage. (**d**) Intralayer Cr the nearest-neighbor (J_1), the second-nearest−neighbor (J_2), and the third-nearest-neighbor (J_3) exchange couplings. (**e**) Interlayer Cr the nearest−neighbor ($J_{1'}$) and the second-nearest-neighbor ($J_{2'}$) exchange couplings in bilayer $Cr_2Ge_2T_6$. The calculated MAE per Cr atom and T_C as functions of strain for (**f**) monolayer and (**g**) bilayer $Cr_2Ge_2T_6$. (**h**) Temperature-dependent MFM examination of curved wrinkles with increasing strain: Left, Topography of three different strained wrinkles. Right, MFM image series depicting enhanced magnetic signal at the wrinkles depending on specific strain state up to RT. Magnetic signals in wrinkles exhibiting strain of 1.3% disappear above 100 K, while wrinkles with 2.3% strain exhibit clear MFM phase signals up to RT. Diagonal periodic lines in the figures are a result of instrument noise and are not part of the magnetic signal (1.3% strain at 110 K and 2.3% strain at 120 K). (Reproduced with permission from [42]. Copyright 2022, American Chemical Society).

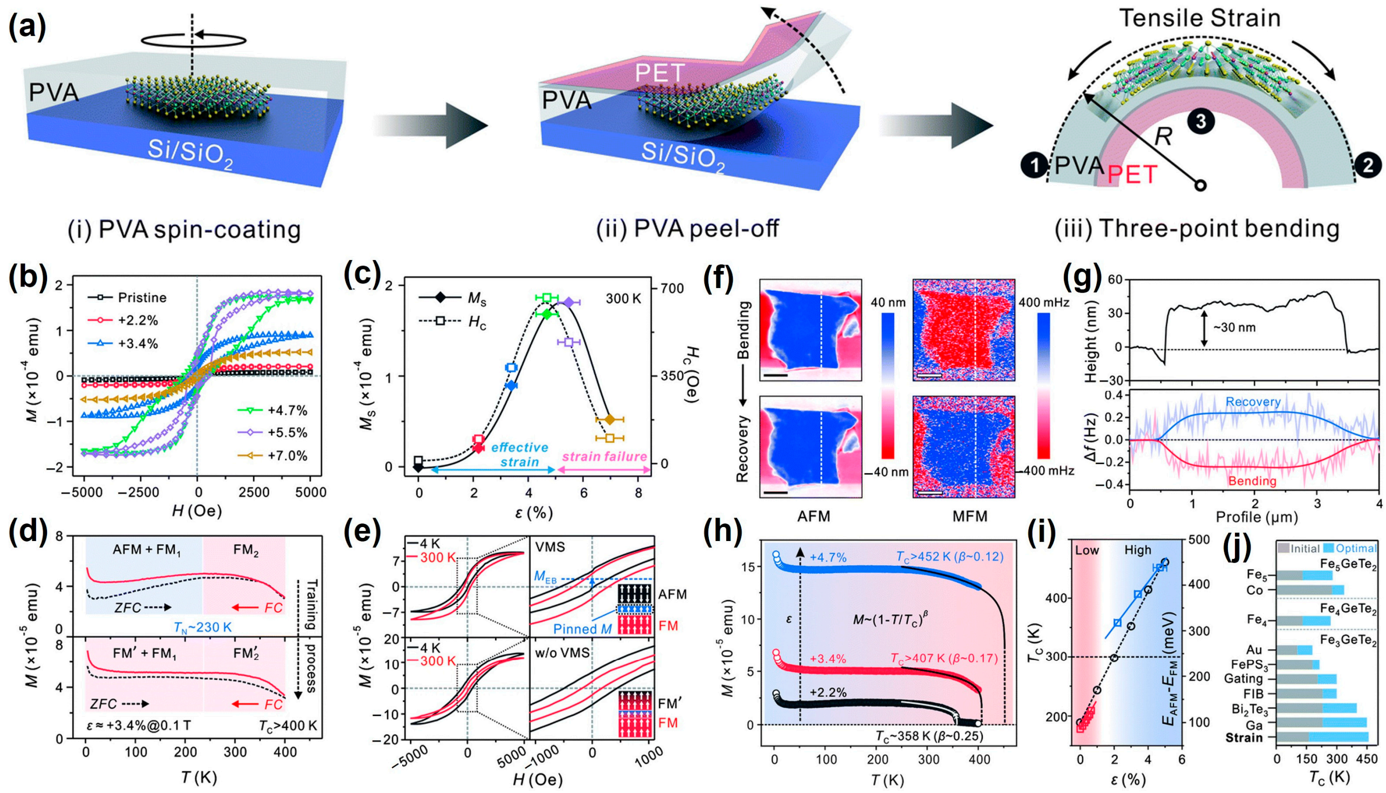

Figure 10. (**a**) Schematic illustration of the transfer and bending process of FGT nanoflakes on flexible PVA/PET substrates. (**b**) *M*–*H* curves at under different strain values. (**c**) Extracted M_S and H_C as a function of tensile strain. (**d**) ZFC and FC curves before and after the training procedure. (**e**) *M*–*H* curves and anomalous exchange-bias effect. Insets are the corresponding schematic illustrations. (**f**) AFM and MFM images of a single nanoflake in the bending and recovery states. All scale bars are 1 mm. (**g**) Extracted height and Df along the white dashed lines marked in (**f**). (**h**) *M*-*T* and critical fittings under different strains. (**i**) Strain-tuned T_C phase diagram. The blue square symbols are the results of this current work and others are collected from the literature. (**j**) Comparison of optimal T_C values using different methods based on the FGT system. From top to bottom: Fe$_5$ [111] and Co [123] represent pure and Co-doped Fe$_5$GeTe$_2$, respectively; Fe$_4$ refers to Fe$_4$GeTe$_2$ [124]; Au [125], FePS$_3$ [37] and Bi$_2$Te$_3$ [34] denote the corresponding heterojunctions with Fe$_3$GeTe$_2$. Gating means the electrostatically gated Fe$_3$GeTe$_2$ [126], FIB [127] and Ga [128] are focused ion beam-treated and Ga ion-implanted Fe$_3$GeTe$_2$, respectively. (Reproduced with permission from [121]. Copyright 2021, The Royal Society of Chemistry).

As another typical example, Miao et al. [47] found that when 0.32% uniaxial tensile strain was applied to the FGT nano sheet, its H_c increased by more than 150%. In order to apply strain, they directly exfoliated the FGT nanosheets onto the PI film. By controlling the distance of the needle tip pushed at the center of the substrate, the PI film was bent to apply different uniaxial tensile strains to the FGT sample. The difference of magnetic anisotropy energy was attributed to the strain-mediated FM. More importantly, they realized a magnetization reversal with the limited strain. Similarly, Xu et al. [48] also observed a reversible phase transition from AFM to FM in a CrSBr nanoflake at cryogenic temperature. Their strain equipment consisted of three piezoelectric actuators glued to a titanium flexure element. By cleaving a silicon substrate to form a micrometer-scale gap, the sample was suspended at the gaps. Furthermore, a piezo voltage was used to continuously apply strain reversibly to the CrSBr flake.

3.3. Lattice Mismatch

High-quality, single-crystalline Fe_4GeTe_2 thin films [43] were grown on sapphire substrate by molecular beam epitaxy (MBE). As shown in Figure 11a, the thin films exhibited a rhombohedral structure. During the MBE epitaxy preparation, due to a lattice mismatch of about 20% between the Fe_4GeTe_2 sample and the sapphire substrate, the lattice rotated 30° to form a perfect single crystal.

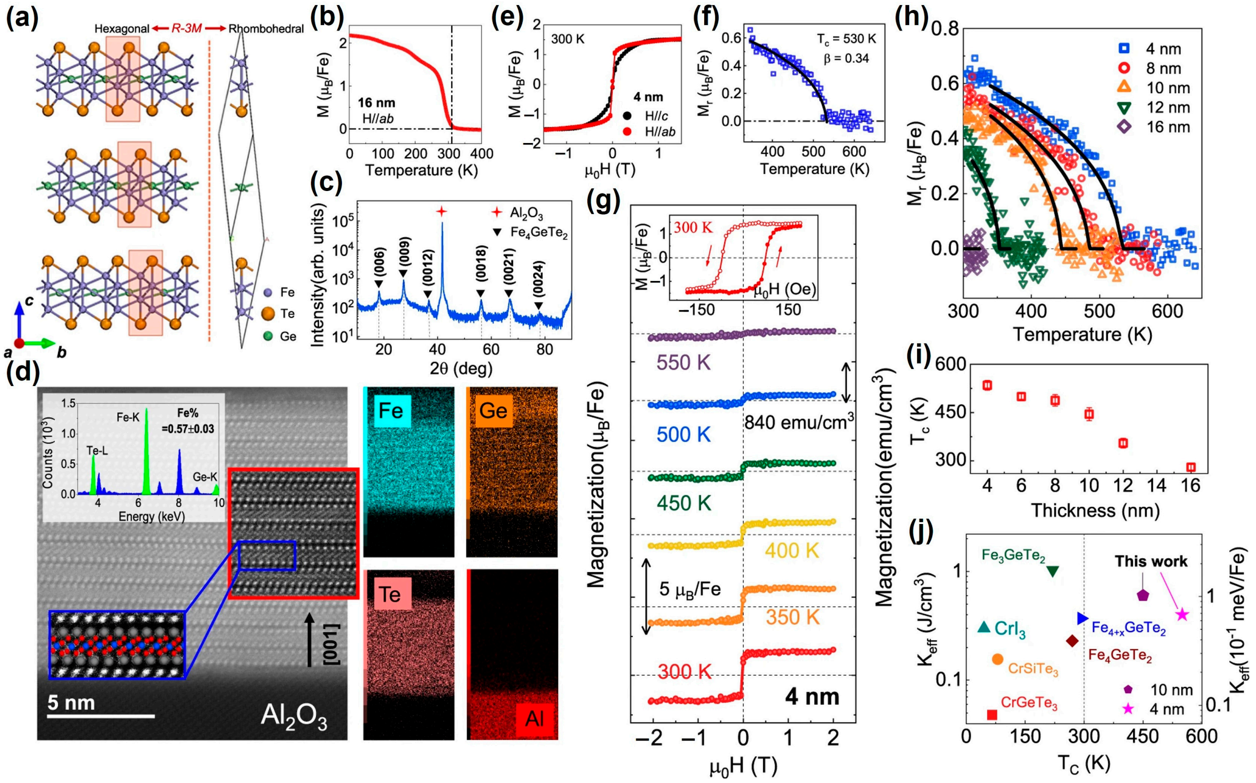

Figure 11. Crystal structure of the Fe_4GeTe_2 and its thickness-dependent magnetism. (**a**) Schematics of the crystal structure of Fe_4GeTe_2 stacked in ABC configuration (**left**), and its rhombohedral structure unit (**right**). (**b**) Temperature dependence of the magnetization for 16 nm Fe_4GeTe_2. (**c**) XRD scan of the Fe_4GeTe_2 film. (**d**) A typical HRTEM image of Fe_4GeTe_2 films; the color squares show the high-pass filtered images of the vdW structure. Up Inset: The EDX result verifies the 4:1:2 Fe: Ge: Te stoichiometric composition with the uniform element distribution map (right). I *M*–*H* curves of 4 nm Fe_4GeTe_2 at 300 K. (**e**) Room-temperature magnetic hysteresis loops. (**f**) In-plane M_r–T curve. (**g**) Detailed magnetic field-dependent magnetization of 4 nm Fe_4GeTe_2 at various temperatures for $H_{//ab}$. Inset: zoom-in hysteresis loop at 300 K. (**h**) M_r-T curves. (**i**) Tc for Fe_4GeTe_2 thin films with different thicknesses. (**j**) Effective magnetic an isotropy energy K_{eff} and curie temperature Tc for our samples and previous vdW ferromagnets [77,124,129–131]. (Reproduced with permission from [43]. Copyright 2023, Springer Nature).

However, there was a tensile strain of about 2% inside the Fe_4GeTe_2 film. The in-plane *M*-*T* curve of the 16 nm FGT film in Figure 11b indicated that its T_C was close to RT. The results of XRD (Figure 11c) and HRTEM (Figure 11d) indicated that the FGT film had a perfect single crystal, and the atomic ratio of the Fe:Ge:Te element was about 4:1:2. At 300 K, a 4 nm film exhibited robust in-plane magnetic anisotropy, as shown in Figure 11e. By fitting the M_r-T curve in Figure 11f, the T_C could be deduced as high as 530 K. Furthermore, in Figure 11, it was confirmed through *M*-*H* loops that the few layered FGT sample exhibited high-temperature FM. In addition, the thickness dependence of T_C showed that when the thickness was thinner, its T_C was higher, as shown in Figure 11h,i. Notably, MBE-prepared FGT had the higher T_C and maintains a relatively high-magnetic anisotropy (Figure 11j).

Through DFT calculations, it was found that a 2% tensile strain was not the reason for the enhanced T_C.

3.4. Electrostatic Force

Considering the abnormally large mechanical response of $Cr_2Ge_2Te_6$ (CGT) thin films caused by strong magnetostriction at T_C, it was expected that this reverse effect could achieve strain-controlled T_C. As shown in Figure 12a–c, the electrostatic strain-tuning T_C was realized in a suspended $Cr_2Ge_2Te_6/WSe_2$ heterostructure [44]. After applying a gate voltage V_g, there was electrostatic force (F_{el}) in Figure 12c between the heterostructure and the bottom silicon substrate, resulting in strain in $Cr_2Ge_2Te_6$ thin films. The strain of the CGT layer can be estimated using the following formula:

$$\begin{aligned} \Delta\epsilon &= \epsilon_{el}(V_g)+\epsilon_b(V_g) \\ &\approx \left[\frac{2}{3}\left(\frac{\varepsilon_0 r}{8g_0{}^2 n(T_0)}\right)^2\right]V_g^4+\left[\frac{\varepsilon_0 r\Delta z(1-v)}{4g_0{}^2 n(T_0)}\right]V_g^2, \end{aligned} \tag{3}$$

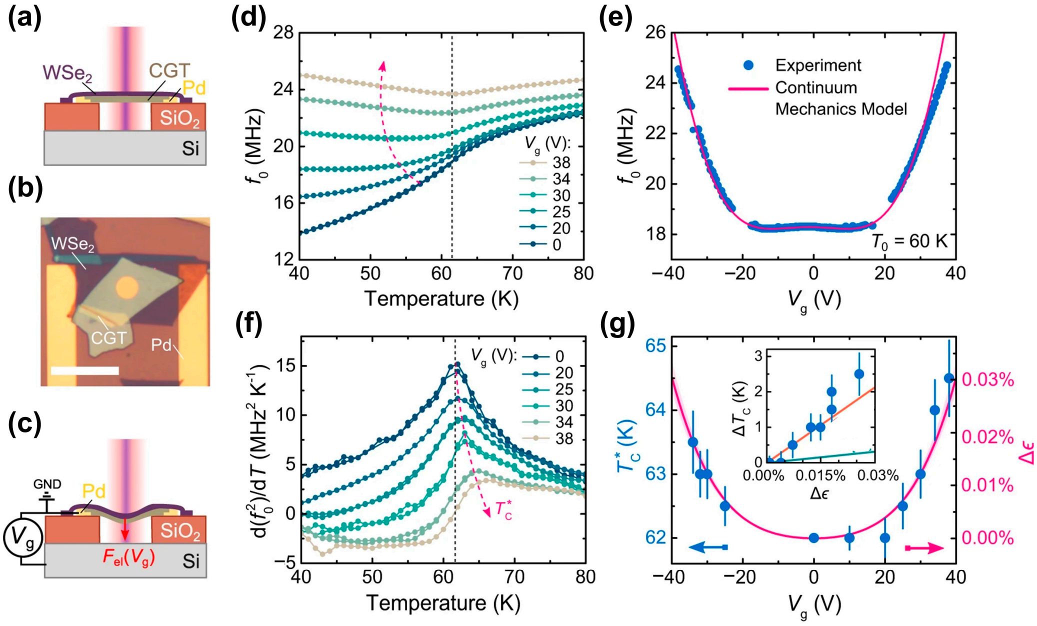

Figure 12. Strain-mediated T_C in a suspended CGT/WSe_2 heterostructure. (**a**) The schematic cross-section of the suspended CGT/WSe_2 heterostructure membrane. (**b**) The optical image of the heterostructure. Scale bar: 12 μm. (**c**) The schematics of the electrostatic strain-tuning principle. (**d**) Measured resonance frequencies f_0 of the heterostructure membrane as a function of temperature for different gate voltages V_g. (**e**) Filled blue circles—the measured resonance frequency as a function of V_g at 60 K. (**f**) The temperature derivative of $f_0{}^2$ as a function of temperature. (**g**) Solid magenta line—the estimate of electrostatically induced strain $\Delta\epsilon$ as a function of V_g. The shaded magenta region shows the uncertainty in $\Delta\epsilon$. The inset shows as a function of added voltage-induced strain $\Delta\epsilon$ in addition to calculations from Li and Yang [73] (solid green line) and from Dong et al. [132] (solid orange line). The vertical error bars in T_C were estimated from determining the peak position in (**e**) within 2% accuracy in the measured maximum. (Reproduced with permission from [44]. Copyright 2022, American Chemical Society).

Note that $\Delta\epsilon$ is the total strain in the CGT layer; ϵ_{el} is the electrostatic pulling strain; ϵ_b is bending strain; ε_0 is the dielectric constant of vacuum; V_g is the gate voltage; r is the membrane radius; v is the Poisson's ratio; $n(T_0)$ is total tension in suspended heterostructures at $T_0 = 60$ K; and g_0 is the separation between the heterostructure and the bottom Si substrate. Interestingly, when the electrostatic force induced a strain of 0.026%, the T_C of the suspended $Cr_2Ge_2Te_6$ /WSe_2 heterostructure was increased by about 2.6 K, as shown in Figure 12d–g.

3.5. Field-Cooling

Due to the fact that the lattice parameters of CGT materials at 5 K are greater than those at 270 K, it would cause in-plane expansion during cooling [133,134]. Phatak et al. [45] found that field-cooling could cause the material expansion in CGT flakes, leading to in-plane strain. Furthermore, they directly observed strain-induced evolution of the magnetic domain structure by cryogenic Lorentz transmission electron microscopy (LTEM), which was closely related to the magnetoelastic coupling between strain and magnetization. This work revealed how to directly measure magnetic domain structures at the nanoscale.

4. Conclusions and Outlook

In this review, we have summarized the recent progress of strain-mediated intrinsic FM in 2D van der Waals materials with long-range order. First, we introduce how to explain the strain-mediated intrinsic FM on Cr-based and Fe-based 2D van der Waals materials with long-range FM order through ab initio Density functional theory (DFT), and how to calculate magnetic anisotropy energy (MAE) and T_C from the interlayer exchange coupling. Subsequently, we focus on numerous attempts to apply strain to 2D materials in experiments, including wrinkle-induced strain, flexible substrate bending or stretching, lattice mismatch, electrostatic force and field-cooling. However, research in this field is still in its early stages and there are many challenges that must be overcome.

By selecting substrates with different thermal expansion coefficients, including x-quartz [135–138], sapphire [27,28,139], and SiO_2 [114]), uniaxial [135–138] or biaxial strain [27,28,114,139,140] could be introduced into 2D materials. The introduction of biaxial strain in this way was limited to the study of 2D materials without intrinsic long-range magnetic order, such as MoS_2 [28] and ReS_2 [27]. So far, this strategy has not been applied to the research on 2D intrinsic van der Waals materials. Very few equipment [47,48,121] could apply strain to 2D materials, but less could be coupled with magnetic testing equipment [41,141]. Especially, it is very challenging that one could accurately determine the strain while measuring the magnetic properties and T_C in different regions.

Recently, some emerging magnetic imaging technologies, such as magneto-optical Kerr effect (MOKE) [7,8,40,142–144], magnetic circular dichroism (MCD) [62,126,145–149], photoemission electron microscopy (PPEM) [150], scanning transmission X-ray microscopy (STXM) [151], Lorentz transmission electron microscopy (LTEM) [150–152], spin-polarized scanning tunneling microscopy (SP-TEM) [66,153], MFM [41,154], scanning SQUID [155–159], and scanning nitrogen-vacancy center microscopy (SNVM) [160–164], have been used to study 2D FM materials. However, these studies have not yet been combined with strain and, currently, it is almost impossible to directly analyze the relationship between strain and FM in 2D intrinsic materials. More importantly, strengthening the guideline of strain-mediated FM will promote the development of spintronics and straintronics.

Author Contributions: Writing—original draft preparation, H.R.; writing—review and editing, H.R. and G.X.; supervision, G.X. All authors have read and agreed to the published version of the manuscript.

Funding: This research was funded by National Natural Science Foundation of China (Grant No. 52172272), Shandong Province Natural Science Foundation (Grant No. ZR202103040767) and Doctoral Scientific Research Foundation of Liaocheng University (Grant No. 318052054).

Institutional Review Board Statement: Not applicable.

Informed Consent Statement: Not applicable.

Data Availability Statement: Not applicable.

Conflicts of Interest: The authors declare no conflict of interest.

Abbreviations

2D	two-dimensional
3D	three-dimensional
AFM	antiferromagnetism
BKT	Berezinskii-Kosterlitz-Thouless
CDW	charge density wave
CGT	$Cr_2Ge_2Te_6$
CPT	$CrPbTe_3$
DFT	density functional theory
DM	Dzialoshinskii-Moriya
DOS	density of states
FGT	Fe_3GeTe_2
FM	ferromagnetism
GGA	the generalized gradient approach
HRTEM	high resolution transmission electron microscopy
LDA	linear density approach
LRO	long-range order
LSDA	local spin density approximation
LTEM	lorentz transmission electron microscopy
MAE	magnetic anisotropy energy
MBE	molecular beam epitaxy
MC	Monte Carlo
MCD	magnetic circular dichroism
MFM	magnetic force microscopy
MOKE	magneto-optical Kerr effect
NM	nonmagnetism
PAD	polymer assisted deposition
PDMS	polydimethylsiloxane
PEEM	photoemission electron microscopy
PET	polyethyleneterephthalate
PI	polyimide
PRA	the random phase approximation
PVA	polyvinyl alcohol
QMC	Quantum Monte Carlo
RT	room temperature
SEM	scanning electron microscopy
SNVM	scanning nitrogen-vacancy center microscopy
SP-TEM	spin-polarized scanning tunneling microscopy
SQUID	superconducting quantum interference device magnetometry
SOC	spin-orbit coupling
SSR	solid-state reaction
STM	scanning tunneling microscopy
STXM	scanning transmission X-ray microscopy
XRD	X-ray diffraction
F_{el}	electrostatic force
T_C	curie temperature
J	the exchange coupling constant
K	magnetic anisotropy
ΔE	total energy difference

References

1. Mermin, N.D.; Wagner, H. Absence of ferromagnetism or antiferromagnetism in one- or two-dimensional isotropic heisenberg models. *Phys. Rev. Lett.* **1966**, *17*, 1133–1136. [CrossRef]
2. Hohenberg, P.C. Existence of long-range order in one and two dimensions. *Phys. Rev.* **1967**, *158*, 383–386. [CrossRef]
3. Meiklejohn, W.H.; Bean, C.P. New magnetic anisotropy. *Phys. Rev.* **1956**, *102*, 1413–1414. [CrossRef]
4. Onsager, L. Crystal statistics. I. a two-dimensional model with an order-disorder transition. *Phys. Rev.* **1944**, *65*, 117–149. [CrossRef]

5. Gibertini, M.; Koperski, M.; Morpurgo, A.F.; Novoselov, K.S. Magnetic 2D materials and heterostructures. *Nat. Nanotechnol.* **2019**, *14*, 408–419. [CrossRef] [PubMed]
6. Wang, Q.H.; Bedoya-Pinto, A.M.; Dismukes, A.H.; Hamo, A.; Jenkins, S.; Koperski, M.; Liu, Y.; Sun, Q.C.; Telford, E.J.; Kim, H.H.; et al. The magnetic genome of two-dimensional van der Waals materials. *ACS Nano* **2022**, *16*, 6960–7079. [CrossRef]
7. Gong, C.; Li, L.; Li, Z.L.; Ji, H.W.; Stern, A.; Xia, Y.; Cao, T.; Bao, W.; Wang, C.Z.; Wang, Y.A.; et al. Discovery of intrinsic ferromagnetism in two-dimensional van der Waals crystals. *Nature* **2017**, *546*, 265–269. [CrossRef]
8. Huang, B.; Clark, G.; Navarro-Moratalla, E.; Klein, D.R.; Cheng, R.; Seyler, K.L.; Zhong, D.; Schmidgall, E.; McGuire, M.A.; Cobden, D.H.; et al. Layer-dependent ferromagnetism in a van der Waals crystal down to the monolayer limit. *Nature* **2017**, *546*, 270–273. [CrossRef]
9. Bissett, M.A.; Tsuji, M.; Ago, H. Strain engineering the properties of graphene and other two-dimensional crystals. *Phys. Chem. Chem. Phys.* **2014**, *16*, 11124–11138. [CrossRef]
10. Roldán, R.; Castellanos-Gomez, A.; Cappelluti, E.; Guinea, F. Strain engineering in semiconducting two-dimensional crystals. *J. Phys. Condens. Matter* **2019**, *27*, 313201. [CrossRef]
11. Luo, M.C.; Guo, S.J. Strain-controlled electrocatalysis on multimetallic nanomaterials. *Nat. Rev. Mater.* **2019**, *2*, 17059. [CrossRef]
12. Bukharaev, A.A.; Zvezdin, K.; Pyatakov, A.P.; Fetisov, Y.K. Straintronics: A new trend in micro- and nanoelectronics and materials science. *Phys.-Usp.* **2018**, *61*, 1175–1212. [CrossRef]
13. Deng, S.K.; Sumant, A.V.; Berry, V. Strain engineering in two-dimensional nanomaterials beyond graphene. *Nano Today* **2018**, *22*, 14–35. [CrossRef]
14. Dai, Z.H.; Liu, L.Q.; Zhang, Z. Strain engineering of 2D materials: Issues and opportunities at the interface. *Adv. Mater.* **2019**, *31*, 1805417. [CrossRef] [PubMed]
15. Xia, Z.H.; Guo, S.J. Strain engineering of metal-based nanomaterials for energy electrocatalysis. *Chem. Soc. Rev.* **2019**, *48*, 3265–3278. [CrossRef] [PubMed]
16. Sun, Y.F.; Liu, K. Strain engineering in functional 2-dimensional materials. *J. Appl. Phys.* **2019**, *125*, 082402. [CrossRef]
17. Peng, Z.W.; Chen, X.L.; Fan, Y.L.; Srolovitz, D.J.; Lei, D.Y. Strain engineering of 2D semiconductors and graphene: From strain fields to band-structure tuning and photonic applications. *Light-Sci. Appl.* **2020**, *9*, 190. [CrossRef]
18. Yan, Y.L.; Ding, S.; Wu, X.N.; Zhu, J.; Feng, D.M.; Yang, X.D.; Li, F.F. Tuning the physical properties of ultrathin transition-metal dichalcogenides via strain engineering. *RSC Adv.* **2020**, *10*, 39455–39467. [CrossRef]
19. Miao, F.; Liang, S.J.; Cheng, B. Straintronics with van der Waals materials. *NPJ Quantum Mater.* **2021**, *6*, 59. [CrossRef]
20. Ren, H.T.; Xiang, G. Morphology-dependent room-temperature ferromagnetism in undoped ZnO nanostructures. *Nanomaterials* **2021**, *11*, 3199. [CrossRef]
21. Yang, S.X.; Chen, Y.J.; Jiang, C.B. Strain engineering of two-dimensional materials: Methods, properties, and applications. *InfoMat* **2021**, *3*, 397–420. [CrossRef]
22. Xu, X.H.; Liang, T.; Kong, D.B.; Wang, B.; Zhi, L.J. Strain engineering of two-dimensional materials for advanced electrocatalysts. *Mater. Today Nano* **2021**, *41*, 100111. [CrossRef]
23. Yang, X.B.; Wang, Y.Y.; Tong, X.L.; Yang, N.J. Strain engineering in electrocatalysts: Fundamentals, progress, and perspectives. *Adv. Energy Mater.* **2022**, *12*, 2102261. [CrossRef]
24. Qi, Y.P.; Sadi, M.A.; Hu, D.; Zheng, M.; Wu, Z.P.; Jiang, Y.C.; Chen, Y.P. Recent progress in strain engineering on van der Waals 2D materials: Tunable electrical, electrochemical, magnetic, and optical properties. *Adv. Mater.* **2023**, *35*, 2205714. [CrossRef] [PubMed]
25. Ren, H.T.; Xiang, G. Strain-modulated magnetism in MoS_2. *Nanomaterials* **2022**, *12*, 1929. [CrossRef] [PubMed]
26. Ren, H.T.; Xiang, G. Recent progress in research on ferromagnetic rhenium disulfide. *Nanomaterials* **2022**, *19*, 3451. [CrossRef]
27. Ren, H.T.; Xiang, G.; Lu, J.T.; Zhang, X.; Zhang, L. Biaxial strain-mediated room temperature ferromagnetism of ReS_2 web buckles. *Adv. Electron. Mater.* **2019**, *5*, 1900814. [CrossRef]
28. Ren, H.T.; Zhang, L.; Xiang, G. Web buckle-mediated room-temperature ferromagnetism in strained MoS_2 thin films. *Appl. Phys. Lett.* **2020**, *116*, 012401. [CrossRef]
29. Novoselov, K.S.; Geim, A.K.; Morozov, S.V.; Jiang, D.; Zhang, Y.; Dubonos, S.V.; Grigorieva, I.V.; Firsov, A.A. Electric field effect in atomically thin carbon films. *Science* **2004**, *306*, 666. [CrossRef]
30. Castellanos-Gomez, A.; Roldan, R.; Cappelluti, E.; Buscema, M.; Guinea, F.; van der Zant, H.S.J.; Steele, G.A. Local strain engineering in atomically rhin MoS_2. *Nano Lett.* **2013**, *13*, 5361–5366. [CrossRef]
31. Lu, P.; Wu, X.J.; Guo, W.L.; Zeng, X.C. Strain-dependent electronic and magnetic properties of MoS_2 monolayer, bilayer, nanoribbons and nanotubes. *Phys. Chem. Chem. Phys.* **2012**, *14*, 13035–13040. [CrossRef] [PubMed]
32. Conley, H.J.; Wang, B.; Ziegler, J.I.; Haglund, R.F.; Pantelides, S.T.; Bolotin, K.I. Bandgap engineering of strained monolayer and bilayer MoS_2. *Nano Lett.* **2013**, *13*, 3626–3630. [CrossRef] [PubMed]
33. Bertolazzi, S.; Brivio, J.; Kis, A. Stretching and breaking of ultrathin MoS_2. *ACS Nano* **2011**, *5*, 9703–9709. [CrossRef]
34. Wang, H.Y.; Liu, Y.J.; Wu, P.C.; Hou, W.J.; Jiang, Y.H.; Li, X.H.; Pandey, C.; Chen, D.D.; Yang, Q.; Wang, H.T.; et al. Above room-temperature ferromagnetism in wafer-scale two-dimensional van der Waals Fe_3GeTe_2 tailored by a topological insulator. *ACS Nano* **2020**, *14*, 10045–10053. [CrossRef] [PubMed]

35. Chen, X.H.; Wang, H.T.; Liu, H.J.; Wang, C.; Wei, G.S.; Fang, C.; Wang, H.C.; Geng, C.Y.; Liu, S.J.; Li, P.Y.; et al. Generation and control of Terahertz spin currents in topology-induced 2D ferromagnetic Fe_3GeTe_2 | Bi_2Te_3 heterostructures. *Adv. Mater.* **2022**, *34*, 2106172. [CrossRef]
36. Dolui, K.; Petrovic, M.D.; Zollner, K.; Plechac, P.; Fabian, J.; Nikolic, B.K. Proximity spin-orbit torque on a two-dimensional magnet within van der Waals heterostructure: Current-driven antiferromagnet-to-ferromagnet reversible nonequilibrium phase transition in Bilayer CrI_3. *Nano Lett.* **2020**, *20*, 2288–2295. [CrossRef]
37. Zhang, L.M.; Huang, X.Y.; Dai, H.W.; Wang, M.S.; Cheng, H.; Tong, L.; Li, Z.; Han, X.T.; Wang, X.; Ye, L.; et al. Proximity-coupling-induced significant enhancement of coercive field and curie temperature in 2D van der Waals heterostructures. *Adv. Mater.* **2020**, *34*, 2002032. [CrossRef]
38. Wang, Z.Y.; Tang, C.; Sachs, R.; Barlas, Y.; Shi, J. Proximity-induced ferromagnetism in graphene revealed by the anomalous hall effect. *Phys. Rev. Lett.* **2015**, *114*, 016603. [CrossRef]
39. Katmis, F.; Lauter, V.; Nogueira, F.S.; Assaf, B.A.; Jamer, M.E.; Wei, P.; Satpati, B.; Freeland, J.W.; Eremin, I.; Heiman, D.; et al. A high-temperature ferromagnetic topological insulating phase by proximity coupling. *Nature* **2016**, *533*, 513–516. [CrossRef]
40. Ciorciaro, L.; Kroner, M.; Watanabe, K.; Taniguchi, T.; Imamoglu, A. Observation of magnetic proximity effect using resonant optical spectroscopy of an electrically tunable $MoSe_2/CrBr_3$ heterostructure. *Phys. Rev. Lett.* **2020**, *124*, 197401. [CrossRef]
41. Yang, S.X.; Wang, C.; Sahin, H.; Chen, H.; Li, Y.; Li, S.S.; Suslu, A.; Peeters, F.M.; Liu, Q.; Li, J.B.; et al. Tuning the optical, magnetic, and electrical properties of $ReSe_2$ by nanoscale strain engineering. *Nano Lett.* **2015**, *15*, 1660–1666. [CrossRef] [PubMed]
42. O'Neill, A.; Rahman, S.; Zhang, Z.; Schoenherr, P.; Yildirim, T.J.; Gu, B.; Su, G.; Lu, Y.R.; Seidel, J. Enhanced room temperature ferromagnetism in highly strained 2D semiconductor $Cr_2Ge_2Te_6$. *ACS Nano* **2023**, *17*, 735–742. [CrossRef]
43. Wang, H.T.; Lu, H.C.; Guo, Z.X.; Li, A.; Wu, P.C.; Li, J.; Xie, W.R.; Sun, Z.M.; Li, P.; Damas, H.; et al. Interfacial engineering of ferromagnetism in wafer-scale van der Waals Fe_4GeTe_2 far above room temperature. *Nat. Commun.* **2023**, *14*, 2483. [CrossRef] [PubMed]
44. Šiškins, M.; Kurdi, S.; Lee, M.; Slotboom, B.J.M.; Xing, W.Y.; l Mañas-Valero, S.; Coronado, E.; Jia, S.; Han, W.; Sar, T.V.D.; et al. Nanomechanical probing and strain tuning of the curie temperature in suspended $Cr_2Ge_2Te_6$-based heterostructures. *NPJ 2D Mater. Appl.* **2022**, *6*, 41. [CrossRef]
45. McCray, A.R.C.; Li, Y.; Qian, E.; Li, Y.; Wang, W.; Huang, Z.J.; Ma, X.M.; Liu, Y.Z.; Chung, D.Y.; Kanatzidis, M.G.; et al. Direct observation of magnetic bubble lattices and magnetoelastic effects in van der Waals $Cr_2Ge_2Te_6$. *Adv. Funct. Mater.* **2023**, *23*, 2214203. [CrossRef]
46. Noah, A.; Zur, Y.; Fridman, N.; Singh, S.; Gutfreund, A.; Herrera, E.; Vakahi, A.; Remennik, S.; Huber, M.E.; Gazit, S.; et al. Nano-patterned magnetic edges in $CrGeTe_3$ for quasi 1-D spintronic devices. *ACS Appl. Nano Mater.* **2023**, *6*, 8627–8634. [CrossRef]
47. Yu, W.; Wang, C.; Liang, S.J.; Ma, Z.C.; Xu, K.; Liu, X.W.; Zhang, L.L.; Admasu, A.S.; Cheong, S.W.; Wang, L.Z.; et al. Strain-sensitive magnetization reversal of a van der Waals magnet. *Adv. Mater.* **2020**, *23*, 2004533.
48. Cenker, J.; Sivakumar, S.; Xie, K.C.; Miller, A.; Thijssen, P.; Liu, Z.Y.; Dismukes, A.; Fonseca, J.; Anderson, E.; Zhu, X.Y.; et al. Reversible strain-induced magnetic phase transition in a van der Waals magnet. *Nat. Nanotechnol.* **2022**, *17*, 256–261. [CrossRef]
49. Rahman, S.; Torres, J.F.; Khan, A.R.; Lu, Y.R. Recent developments in van der Waals antiferromagnetic 2D materials: Synthesis, characterization, and device implementation. *ACS Nano* **2021**, *15*, 17175–17213. [CrossRef]
50. Liu, Y.P.; Zeng, C.; Zhong, J.H.; Ding, J.N.; Wang, Z.M.; Liu, Z.W. Spintronics in two-dimensional materials. *Nan-Micro Lett.* **2020**, *12*, 93. [CrossRef]
51. Mak, K.; Shan, J.; Ralph, D.C. Probing and controlling magnetic states in 2D layered magnetic materials. *Nat. Rev. Phys.* **2019**, *1*, 646–661. [CrossRef]
52. Marchiori, E.; Ceccarelli, L.; Rossi, N.; Lorenzelli, L.; Degen, C.L.; Poggio, M. Nanoscale magnetic field imaging for 2D materials. *Nat. Rev. Phys.* **2021**, *4*, 49–60. [CrossRef]
53. Li, W.; Yang, Z.Y.; Hou, Y.L.; Gao, S. Controllable preparation and magnetism control of two-dimensional magnetic nanomaterials. *Rrog. Chem.* **2020**, *32*, 1437–1451.
54. Xing, S.C.; Zhou, J.; Zhang, X.G.; Elliott, S.; Sun, Z.M. Theory, properties and engineering of 2D magnetic materials. *Rrog. Mater. Sci.* **2023**, *132*, 101036. [CrossRef]
55. Ningrum, V.P.; Liu, B.W.; Wang, W.; Yin, Y.; Cao, Y.; Zha, C.Y.; Xie, H.G.; Jiang, X.H.; Sun, Y.; Qin, S.C.; et al. Recent advances in two-dimensional magnets: Physics and devices towards spintronic applications. *Research* **2020**, *2020*, 1768918. [CrossRef]
56. Gong, C.; Zhang, X. Two-dimensional magnetic crystals and emergent heterostructure devices. *Science* **2019**, *363*, 6428. [CrossRef] [PubMed]
57. Dai, C.Y.; He, P.; Luo, L.X.; Zhan, P.X.; Guan, B.; Zheng, J. Research progress of two-dimensional magnetic materials. *Sci. China. Mater.* **2023**, *66*, 859–876. [CrossRef]
58. Zhang, W.B.; Qu, Q.; Zhu, P.; Lam, C.H. Robust intrinsic ferromagnetism and half semiconductivity in stable two-dimensional single-layer chromium trihalides. *J. Phys. Chem. C* **2015**, *3*, 12457–12468. [CrossRef]
59. Webster, L.; Yan, J.A. Strain-tunable magnetic anisotropy in monolayer $CrCl_3$, $CrBr_3$, and CrI_3. *Phys. Rev. B* **2018**, *98*, 144411. [CrossRef]
60. Wang, Z.; Gibertini, M.; Dumcenco, D.; Taniguchi, T.; Watanabe, K.; Giannini, E.; Morpurgo, A.F. Determining the phase diagram of atomically thin layered antiferromagnet $CrCl_3$. *Nat. Nanotechnol.* **2019**, *14*, 1116–1122. [CrossRef]

61. Ahmad, A.S.; Liang, Y.C.; Dong, M.D.; Zhou, X.F.; Fang, L.M.; Xia, Y.H.; Dai, J.H.; Yan, X.Z.; Yu, X.H.; Dai, J.F.; et al. Pressure-driven switching of magnetism in layered $CrCl_3$. *Nanoscale* **2020**, *12*, 22935–22944. [CrossRef] [PubMed]
62. Bedoya-Pinto, A.; Ji, J.R.; Pandeya, A.K.; Gargiani, P.; Valvidares, M.; Sessi, P.; Taylor, J.M.; Radu, F.; Chang, K.; Parkin, S.S.P. Intrinsic 2D-XY Ferromagnetism in a van der Waals monolayer. *Science* **2021**, *374*, 616–620. [CrossRef] [PubMed]
63. Dupont, M.; Kvashnin, Y.O.; Shiranzaei, M.; Fransson, J.; Laflorencie, N.; Kantian, A. Monolayer $CrCl_3$ as an ideal test bed for the universality classes of 2D magnetism. *Phys. Rev. Lett.* **2021**, *127*, 037204. [CrossRef]
64. Ebrahimian, A.; Dyrdał, A.; Qaiumzadeh, A. Control of magnetic states and spin interactions in bilayer $CrCl_3$ with strain and electric fields: An ab initio study. *Sci. Rep.* **2023**, *13*, 5336. [CrossRef] [PubMed]
65. Liu, J.; Mo, P.H.; Shi, M.C.; Gao, D.; Jiwu Lu, J.W. Multi-scale analysis of strain-dependent magnetocrystalline anisotropy and strain-induced villari and nagaoka-honda effects in a two-dimensional ferromagnetic chromium tri-iodide monolayer. *J. Appl. Phys.* **2018**, *124*, 044303. [CrossRef]
66. Sivadas, N.; Okamoto, S.; Xu, X.D.; Fennie, C.J.; Xiao, D. Stacking-dependent magnetism in bilayer CrI_3. *Nano Lett.* **2018**, *18*, 7658–7664. [CrossRef]
67. Li, T.X.; Jiang, S.W.; Sivadas, N.; Wang, Z.F.; Xu, Y.; Weber, D.; Goldberger, J.E.; Watanabe, K.; Taniguchi, T.; Fennie, C.J.; et al. Pressure-controlled interlayer magnetism in atomically thin CrI_3. *Nat. Mater.* **2019**, *18*, 1303–1308. [CrossRef]
68. Song, T.C.; Fei, Z.Y.; Yankowitz, M.; Lin, Z.; Jiang, Q.N.; Hwangbo, K.; Zhang, Q.; Sun, B.S.; Taniguchi, T.; Watanabe, K.; et al. Switching 2D magnetic states via pressure tuning of layer stacking. *Nat. Mater.* **2019**, *18*, 1298–1302. [CrossRef]
69. Wu, Z.W.; Yu, J.; Yuan, S.J. Strain-tunable magnetic and electronic properties of monolayer CrI_3. *Phys. Chem. Chem. Phys.* **2019**, *21*, 7750–7755. [CrossRef]
70. Leon, A.M.; Gonzalez, J.W.; Mejia-Lopez, J.; Lima, F.C.D.; Morell, E.S. Strain-induced phase transition in CrI_3 bilayers. *2D Mater.* **2020**, *7*, 035008. [CrossRef]
71. Vishkayi, S.I.; Torbatian, Z.; Qaiumzadeh, A.; Asgari, R. Strain and electric-field control of spin-spin interactions in monolayer CrI_3. *Phys. Rev. Mater.* **2020**, *4*, 094004. [CrossRef]
72. Safi, A.L.; Chakraborty, S.; Ahmed, M.A.; Chattopadhyay, B. Strain tunable electronic band structure and magnetic anisotropy of CrI_3 bilayer. *ECS J. Solid State Sci. Technol.* **2022**, *11*, 063008. [CrossRef]
73. Li, X.X.; Yang, J.L. $CrXTe_3$ (X = Si, Ge) nanosheets: Two dimensional intrinsic ferromagnetic semiconductors. *J. Phys. Chem. C* **2014**, *2*, 7071–7076. [CrossRef]
74. Zhuang, H.L.; Xie, Y.; Kent, P.R.C.; Ganesh, P. Computational discovery of ferromagnetic semiconducting single-Layer $CrSnTe_3$. *Phys. Rev. B* **2015**, *92*, 035407. [CrossRef]
75. Dong, X.J.; You, J.Y.; Gu, B.; Su, G. Strain-induced room-temperature ferromagnetic semiconductors with large anomalous hall conductivity in two-dimensional $Cr_2Ge_2Se_6$. *Phys. Rev. Appl.* **2019**, *12*, 014020. [CrossRef]
76. Idzuchi, H.; Llacsahuanga Allcca, A.E.; Pan, X.C.; Tanigaki, K.; Chen, Y.P. Increased curie temperature and enhanced perpendicular magneto anisotropy of $Cr_2Ge_2Te_6$/NiO heterostructures. *Appl. Phys. Lett.* **2019**, *115*, 232403. [CrossRef]
77. Zeisner, J.; Alfonsov, A.; Selter, S.; Aswartham, S.; Ghimire, M.P.; Richter, M.; van den Brink, J.; Büchner, B.; Kataev, V. Magnetic anisotropy and spin-polarized two-dimensional electron gas in the van der Waals ferromagnet $Cr_2Ge_2Te_6$. *Phys. Rev. B* **2019**, *99*, 165109. [CrossRef]
78. Khan, I.; Hong, J.S. High curie temperature and strain-induced semiconductor-metal transition with spin reorientation transition in 2D $CrPbTe_3$ monolayer. *Nanotechnology* **2020**, *31*, 195704. [CrossRef]
79. Selter, S.; Bastien, G.; Wolter, A.U.B.; Aswartham, S.; Büchner, B. Magnetic anisotropy and low-field magnetic phase diagram of the quasi-two-dimensional ferromagnet $Cr_2Ge_2Te_6$. *Phys. Rev. B* **2020**, *101*, 014440. [CrossRef]
80. Spachmann, S.; Selter, S.; Büchner, B.; Aswartham, S.; Klingeler, R. Strong uniaxial pressure dependencies evidencing spin-lattice coupling and spin fluctuations in $Cr_2Ge_2Te_6$. *Phys. Rev. B* **2023**, *107*, 184421. [CrossRef]
81. Deiseroth, H.J.; Aleksandrov, K.; Reiner, C.; Kienle, L.; Kremer, R.K. Fe_3GeTe_2 and Ni_3GeTe_2 -two new layered transition-metal compounds: Crystal structures, HRTEM investigations, and magnetic and electrical properties. *Eur. J. Inorg. Chem.* **2006**, *2006*, 1561–1567. [CrossRef]
82. Zhuang, H.L.; Kent, P.R.C.; Hennig, R.G. Strong anisotropy and magnetostriction in the two-dimensional stoner ferromagnet Fe_3GeTe_2. *Phys. Rev. B* **2016**, *93*, 134407. [CrossRef]
83. Joe, M.; Yang, U.; Lee, C.G. First-principles study of ferromagnetic metal Fe_5GeTe_2. *Nano Mater. Sci.* **2009**, *1*, 299–303. [CrossRef]
84. Li, X.L.; Lu, J.T.; Zhang, J.; You, L.; Su, Y.R.; Tsymbal, E.Y. Spin-dependent transport in van der Waals magnetic tunnel junctions with Fe_3GeTe_2 electrodes. *Nano Lett.* **2019**, *19*, 5133–5139. [CrossRef] [PubMed]
85. Hu, X.H.; Zhao, Y.H.; Shen, X.D.; Krasheninnikov, A.V.; Chen, Z.F.; Sun, L.T. Enhanced ferromagnetism and tunable magnetism in Fe_3GeTe_2 monolayer by strain engineering. *ACS Appl. Mater. Inter.* **2020**, *12*, 26367–26373. [CrossRef]
86. Zhu, M.M.; You, Y.R.; Xu, G.Z.; Tang, J.X.; Gong, Y.Y.; Xu, F. Strain modulation of magnetic coupling in the metallic van der Waals magnet Fe_3GeTe_2. *Intermetallics* **2021**, *131*, 107085. [CrossRef]
87. Chen, D.; Sun, W.; Wang, W.X.; Li, X.N.; Li, H.; Cheng, Z.X. Twist-stacked 2D bilayer Fe_3GeTe_2 with tunable magnetism. *J. Mater. Chem. C* **2022**, *10*, 12741–12750. [CrossRef]
88. Ouvrard, G.; Brec, R. Modification of the cationic ordering with respect to the chalcogen in the layered $MM'P_2X_6$ phases. synthesis and structure of two-dimensional $AgVP_2Se_6$. *Mat. Res. Bull.* **1988**, *23*, 1199–1209. [CrossRef]

89. Song, Z.G.; Sun, X.T.; Zheng, J.X.; Pan, F.; Hou, Y.L.; Yung, M.H.; Yang, J.B.; Lu, J. Spontaneous valley splitting and valley pseudospin field effect transistors of monolayer VagP2Se$_6$. *Nanoscale* **2018**, *10*, 13986–13993. [CrossRef]
90. Peng, Y.X.; Cheng, X.; Gu, P.F.; Wang, F.G.; Yang, J.; Xue, M.Z.; Yang, W.Y.; Wang, C.S.; Liu, S.Q.; Watanabe, K.; et al. A quaternary van der Waals ferromagnetic semiconductor AgVP$_2$Se6. *Adv. Funct. Mater.* **2020**, *30*, 1910036. [CrossRef]
91. Joolee, S.; Son, S.; Park, P.; Kim, M.; Tao, Z.; Oh, J.; Lee, T.; Lee, S.; Kim, J.; Zhang, K.X.; et al. Air-stable and layer-dependent ferromagnetism in atomically thin van der Waals CrPS$_4$. *ACS Nano* **2021**, *15*, 16904–16912.
92. Sadhukhan, B.; Bergman, A.; Kvashnin, Y.O.; Hellsvik, J.; Delin, A. Spin-lattice couplings in two-dimensional CrI$_3$ from first-principles computations. *Phys. Rev. B* **2022**, *105*, 104418. [CrossRef]
93. Kashin, I.V.; Mazurenko, V.V.; Katsnelson, M.I.; Rudenko, A.N. Orbitally-resolved ferromagnetism of monolayer CrI$_3$. *2D Mater.* **2020**, *7*, 025036. [CrossRef]
94. Soriano, D.; Rudenko, A.N.; Katsnelson, M.I.; Rösner, M. Environmental screening and ligand-field effects to magnetism in CrI$_3$ monolayer. *NPJ 2D Comput. Mater.* **2021**, *7*, 162. [CrossRef]
95. Esteras, D.L.; Rybakov, A.; Ruiz, A.M.; Baldoví, J.J. Magnon straintronics in the 2D van der Waals ferromagnet CrSBr from first-principles. *Nano Lett.* **2022**, *22*, 8771–8778. [CrossRef]
96. Kvashnin, Y.O.; Bergman, A.; Lichtenstein, A.I.; Katsnelson, M.I. Relativistic exchange interactions in CrX$_3$ (X=Cl, Br, I) monolayers. *Phys. Rev. B* **2020**, *102*, 115162. [CrossRef]
97. Torelli, D.; Olsen, T. Calculating critical temperatures for ferromagnetic order in two-dimensional materials. *2D Mater.* **2019**, *6*, 015028. [CrossRef]
98. Şaşıoğlu, E.; Sandratskii, L.M.; Bruno, P. First-principles calculation of the intersublattice exchange interactions and curie temperatures of the full heusler alloys Ni$_2$MnX (X=Ga, In, Sn, Sb). *Phys. Rev. B* **2004**, *70*, 024427. [CrossRef]
99. Singh, S.; Caron, L.; D'Souza, S.W.; Fichtner, T.; Porcari, G.; Fabbrici, S.; Shekhar, C.; Chadov, S.; Solzi, M.; Felser, C. Large magnetization and reversible magnetocaloric effect at the second-order magnetic transition in Heusler materials. *Adv. Mater.* **2016**, *28*, 3321–3325. [CrossRef]
100. Chang, C.; Chen, W.; Chen, Y.; Chen, Y.H.; Chen, Y.; Ding, F.; Fan, C.H.; Fan, H.J.; Fan, Z.; Gong, C.; et al. Recent progress on two-dimensional materials. *Acta Phys.-Chim. Sin.* **2021**, *37*, 2108017. [CrossRef]
101. Ghosh, S.; Ershadrad, S.; Borisov, V.; Sanyal, B. Unraveling effects of electron correlation in two-dimensional Fe$_n$GeTe$_2$ (N = 3, 4, 5) by dynamical mean field theory. *NPJ 2D Comput. Mater.* **2023**, *9*, 86. [CrossRef]
102. Kim, K.S.; Zhao, Y.; Jang, H.; Lee, S.Y.; Kim, J.M.; Kim, K.S.; Ahn, J.H.; Kim, P.; Choi, J.Y.; Hong, B.H. Large-scale pattern growth of graphene films for stretchable transparent electrodes. *Nature* **2009**, *457*, 706–710. [CrossRef]
103. Liu, J.Y.; Sun, Q.; Kawazoe, Y.; Jena, P. Exfoliating biocompatible ferromagnetic Cr-trihalide monolayers. *Phys. Chem. Chem. Phys.* **2016**, *13*, 8777–8784. [CrossRef] [PubMed]
104. Guo, H.Y.; Lu, N.; Wang, L.; Wu, X.J.; Zeng, X.C. Tuning electronic and magnetic properties of early transition-metal dichalcogenides via tensile strain. *J. Phys. Chem. C* **2014**, *118*, 7242–7249. [CrossRef]
105. Lv, H.Y.; Lu, W.J.; Shao, D.F.; Liu, Y.; Sun, Y.P. Strain-controlled switch between ferromagnetism and antiferromagnetism in CrSeTe monolayers. *Phys. Rev. B* **2015**, *92*, 214419. [CrossRef]
106. Liu, Y.H.; Kwon, S.; de Coster, G.J.; Lake, R.K.; Neupane, M.R. Structural, electronic, and magnetic properties of CrTe$_2$. *Phys. Rev. Mater.* **2022**, *6*, 084004. [CrossRef]
107. Fumega, A.O.; Phillips, J.; Victor Pardo, V. Controlled two-dimensional ferromagnetism in 1T–CrTe$_2$: The role of charge density wave and strain. *J. Phys. Chem. C* **2020**, *124*, 21047–21053. [CrossRef]
108. Song, Y.; Wang, X.C.; Mi, W.B. Role of electron filling in the magnetic anisotropy of monolayer WSe$_2$ doped with 5*d* transition metals. *Phys. Rev. Mater.* **2017**, *1*, 074408. [CrossRef]
109. Liu, J.; You, Y.R.; Batashev, I.; Gong, Y.Y.; You, X.M.; Huang, B.W.; Zhang, F.Q.; Miao, X.F.; Xu, F.; van Dijk, N.; et al. Design of reversible low-field magnetocaloric effect at room temperature in hexagonal Mn Ferromagnets. *Phys. Rev. Appl.* **2020**, *13*, 054003. [CrossRef]
110. Stahl, J.; Shlaen, E.; Johrendt, D. The van der Waals ferromagnets Fe$_{5\text{-}\delta}$GeTe$_2$ and Fe$_{5\text{-}\delta\text{-}X}Ni_x$GeTe$_2$ -crystal structure, stacking faults, and magnetic properties. *Z. Anorg. Allg. Chem.* **2018**, *644*, 1923–1929. [CrossRef]
111. May, A.F.; Ovchinnikov, D.; Zheng, Q.; Hermann, R.; Calder, S.; Huang, B.V.; Fei, Z.Y.; Liu, Y.H.; Xu, X.D.; McGuire, M.A. Ferromagnetism near room temperature in the cleavable van der Waals crystal Fe$_5$GeTe$_2$. *ACS Nano* **2019**, *13*, 4436–4442. [CrossRef] [PubMed]
112. Dhakal, K.P.; Roy, S.; Jang, H.; Chen, X.; Yun, W.S.; Kim, H.; Lee, J.D.; Kim, J.; Ahn, J.H. Local strain induced band gap modulation and photoluminescence enhancement of multilayer transition metal dichalcogenides. *Chem. Mater.* **2017**, *29*, 5124–5133. [CrossRef]
113. Iguiniz, N.; Frisenda, R.; Bratschitsch, R.; Castellanos-Gomez, A. Revisiting the buckling metrology method to determine the Young's modulus of 2D materials. *Adv. Mater.* **2019**, *31*, 1807150. [CrossRef]
114. Liu, Z.; Amani, M.; Najmaei, S.; Xu, Q.; Zou, X.L.; Zhou, W.; Yu, T.; Qiu, C.Q.; Glen Birdwell, A.; Crowne, F.J.; et al. Strain and structure heterogeneity in MoS$_2$ atomic layers grown by chemical vapour deposition. *Nat. Commun.* **2014**, *5*, 5246. [CrossRef]
115. Brennan, C.J.; Nguyen, J.; Yu, E.T.; Lu, N.S. Interface adhesion between 2D materials and elastomers measured by buckle delaminations. *Adv. Mater. Interfaces* **2015**, *2*, 1500176. [CrossRef]

116. Plechinger, G.; Castellanos-Gomez, A.; Buscema, M.; van der Zant, H.S.J.; Steele, G.A.; Kuc, A.; Heine, T.; Schüller, C.; Korn, T. Control of biaxial strain in single-layer molybdenite using local thermal expansion of the substrate. *2D Mater.* **2015**, *2*, 015006. [CrossRef]
117. Yang, R.; Lee, J.; Tang, G.H.; Sankaran, R.M.; Zorman, C.A.; Feng, P.X.L. Tuning optical signatures of single- and few-layer MoS_2 by blown-bubble bulge straining up to fracture. *Nano Lett.* **2017**, *17*, 4568–4575. [CrossRef]
118. Pak, S.; Lee, J.; Lee, Y.W.; Jang, A.R.; Ahn, S.; Ma, K.Y.; Cho, Y.; Hong, J.; Lee, S.; Jeong, H.Y.; et al. Strain-mediated interlayer coupling effects on the excitonic behaviors in an epitaxially grown MoS_2/WS_2 van der Waals heterobilayer. *Nano Lett.* **2017**, *17*, 5634–5640. [CrossRef]
119. John, A.P.; Thenapparambil, A.; Thalakulam, M. Strain-engineering the schottky barrier and electrical transport on MoS_2. *Nanotechnology* **2020**, *31*, 275703. [CrossRef] [PubMed]
120. Thai, K.Y.; Park, I.J.; Kim, B.J.; Hoang, A.T.; Na, Y.; Park, C.U.; Chae, Y.; Ahn, J.H. MoS_2/graphene photodetector array with strain-modulated photoresponse up to the near-infrared regime. *ACS Nano* **2021**, *15*, 12836–12846. [CrossRef] [PubMed]
121. Hu, L.; Zhou, J.; Hou, Z.P.; Su, W.T.; Yang, B.Z.; Li, L.W.; Yan, M. Polymer-buried van der Waals magnets for promising wearable room-temperature spintronics. *Mater. Horiz.* **2021**, *8*, 3306–3314. [CrossRef] [PubMed]
122. Li, Z.W.; Lv, Y.W.; Ren, L.W.; Li, J.; Kong, L.G.; Zeng, Y.J.; Tao, Q.Y.; Wu, R.X.; Ma, H.F.; Zhao, B.; et al. Efficient strain modulation of 2D materials via polymer encapsulation. *Nat. Commun.* **2020**, *11*, 1151. [CrossRef] [PubMed]
123. Tian, C.K.; Pan, F.H.; Xu, S.; Ai, K.; Xia, T.L.; Cheng, P. Tunable magnetic properties in van der Waals crystals $(Fe_{1\text{-}X}Co_X)_5GeTe_2$. *Appl. Phys. Lett.* **2019**, *115*, 232403. [CrossRef]
124. Seo, J.; Kim, D.Y.; An, E.S.; Kim, K.; Kim, G.Y.; Hwang, S.Y.; Kim, D.W.; Jang, B.G.; Kim, H.; Eom, G.; et al. room temperature ferromagnetism in a magnetic metal-rich van der Waals metal. *Sci. Adv.* **2020**, *6*, eaay8912. [CrossRef] [PubMed]
125. Zhang, L.M.; Song, L.Y.; Dai, H.W.; Yuan, J.H.; Wang, M.S.; Huang, X.Y.; Qiao, L.; Cheng, H.; Wang, X.; Ren, W.; et al. Substrate-modulated ferromagnetism of two-dimensional Fe_3GeTe_2. *Appl. Phys. Lett.* **2020**, *116*, 042402. [CrossRef]
126. Deng, Y.J.; Yu, Y.J.; Song, Y.C.; Zhang, J.Z.; Wang, N.Z.; Sun, Z.Y.; Yi, Y.F.; Wu, Y.Z.; Wu, S.W.; Zhu, J.Y.; et al. Gate-tunable room-temperature ferromagnetism in two-dimensional Fe_3GeTe_2. *Nature* **2018**, *563*, 94–99. [CrossRef]
127. Li, Q.; Yang, M.M.; Gong, C.; Chopdekar, R.V.; N'Diaye, A.T.; Turner, J.; Chen, G.; Scholl, A.; Shafer, P.; Arenholz, E.; et al. Patterning-induced ferromagnetism of Fe_3GeTe_2 van der Waals materials beyond room temperature. *Nano Lett.* **2018**, *18*, 5974–5980. [CrossRef]
128. Yang, M.M.; Li, Q.; Chopdekar, R.V.; Stan, C.; Cabrini, S.; Choi, J.W.; Wang, S.; Wang, T.Y.; Gao, N.; Scholl, A.; et al. Highly enhanced curie temperature in Ga-implanted Fe_3GeTe_2 van der Waals material. *Adv. Quantum Technol.* **2020**, *3*, 2000017. [CrossRef]
129. Niu, W.; Zhang, X.Q.; Wang, W.; Sun, J.B.; Xu, Y.B.; He, L.; Liu, W.Q.; Pu, Y. Probing the atomic-scale ferromagnetism in van der Waals magnet $CrSiTe_3$. *Appl. Phys. Lett.* **2021**, *119*, 172402. [CrossRef]
130. Kim, D.; Park, S.; Lee, J.; Yoon, J.; Joo, S.; Kim, T.; Min, K.J.; Park, S.Y.; Kim, C.; Moon, K.W.; et al. Antiferromagnetic coupling of van der Waals ferromagnetic Fe_3GeTe_2. *Nanotechnology* **2019**, *30*, 245701. [CrossRef]
131. Ribeiro, M.; Gentile, G.; Marty, A.; Dosenovic, D.; Okuno, H.; Vergnaud, C.; Jacquot, J.F.; Jalabert, D.; Longo, D.; Ohresser, P.; et al. Large-scale epitaxy of two-dimensional van der Waals room-temperature ferromagnet Fe_5GeTe_2. *NPJ 2D Mater. Appl.* **2022**, *6*, 10. [CrossRef]
132. Dong, X.J.; You, J.Y.; Zhang, Z.; Gu, B.; Su, G. Great enhancement of curie temperature and magnetic anisotropy in two-dimensional van der Waals magnetic semiconductor heterostructures. *Phys. Rev. B* **2020**, *102*, 144443. [CrossRef]
133. Carteaux, V.; Brunet, D.; Ouvrard, G.; Andre, G. Crystallographic, magnetic and electronic structures of a new layered ferromagnetic compound $Cr_2Ge_2Te_6$. *J. Phys. Condens. Matter* **1995**, *7*, 69. [CrossRef]
134. Spachmann, S.; Elghandour, A.; Selter, S.; Büchner, B.; Aswartham, S.; Klingeler, R. Strong effects of uniaxial pressure and short-range correlations in $Cr_2Ge_2Te_6$. *Phys. Rev. Res.* **2022**, *4*, L022040. [CrossRef]
135. Wang, J.W.; Han, M.J.; Wang, Q.; Ji, Y.Q.; Zhang, X.; Shi, R.; Wu, Z.F.; Zhang, L.; Amini, A.; Guo, L.; et al. Strained epitaxy of monolayer transition metal dichalcogenides for wrinkle arrays. *ACS Nano* **2021**, *15*, 6633–6644. [CrossRef] [PubMed]
136. Wang, E.Z.; Chen, Z.K.; Shi, R.; Xiong, Z.X.; Xin, Z.X.; Wang, B.L.; Guo, J.; Peng, R.X.; Wu, Y.H.; Li, C.Y.; et al. Humidity-controlled dynamic engineering of buckling dimensionality in MoS_2 thin films. *ACS Nano* **2022**, *16*, 14157–14167. [CrossRef]
137. Wang, J.W.; Luo, Y.; Cai, X.B.; Shi, R.; Wang, W.J.; Li, T.R.; Wu, Z.F.; Zhang, X.; Peng, O.W.; Amini, A.; et al. Multiple regulation over growth direction, band structure, and dimension of monolayer WS_2 by a quartz substrate. *Chem. Mater.* **2020**, *32*, 2508–2517. [CrossRef]
138. Wang, E.Z.; Xiong, Z.X.; Chen, Z.K.; Xin, Z.Q.; Ma, H.C.; Ren, H.T.; Wang, B.L.; Guo, J.; Sun, Y.F.; Wang, X.W.; et al. Water nanolayer facilitated solitary-wave-like blisters in MoS_2 thin films. *Nat. Commun.* **2023**, *14*, 4324. [CrossRef]
139. Ren, H.T.; Xiong, Z.X.; Wang, E.Z.; Yuan, Z.Q.; Sun, Y.F.; Zhu, K.L.; Wang, B.L.; Wang, X.W.; Ding, H.Y.; Liu, P.; et al. Watching dynamic self-assembly of web buckles in strained MoS_2 thin films. *ACS Nano* **2019**, *13*, 3106–3116. [CrossRef]
140. Ahn, G.H.; Amani, M.; Rasool, H.; Lien, D.H.; Mastandrea, J.P.; Ager, J.W.; Dubey, M.; Chrzan, D.C.; Minor, A.M.; Javey, A. Strain-engineered growth of two-dimensional materials. *Nat. Commun.* **2017**, *8*, 608. [CrossRef]
141. Li, H.; Qi, X.; Wu, J.; Zeng, Z.; Wei, J.; Zhang, H. Investigation of MoS_2 and graphene nanosheets by magnetic force microscopy. *ACS Nano* **2013**, *7*, 2842–2849. [CrossRef] [PubMed]

142. Kezilebieke, S.; Silveira, O.J.; Huda, M.N.; Vaňo, V.; Aapro, M.; Ganguli, S.C.; Lahtinen, J.; Mansell, R.; Dijken, S.V.; Foster, A.S.; et al. Electronic and magnetic characterization of epitaxial $CrBr_3$ monolayers on a superconducting substrate. *Adv. Mater.* **2021**, *33*, 2006850. [CrossRef] [PubMed]
143. Kerr, J.X. On rotation of the plane of polarization by reflection from the pole of a magnet. *London Edinb. Dublin Philos. Mag. J. Sci.* **1877**, *3*, 321–343. [CrossRef]
144. Wang, Z.; Zhang, T.Y.; Ding, M.; Dong, B.J.; Li, Y.X.; Chen, M.L.; Li, X.X.; Huang, J.Q.; Wang, H.W.; Zhao, X.T.; et al. Electric-field control of magnetism in a few-layered van der Waals ferromagnetic semiconductor. *Nat. Nanotechnol.* **2018**, *13*, 554–559. [CrossRef]
145. Fei, Z.Y.; Huang, B.; Malinowski, P.; Wang, W.B.; Song, T.C.; Sanchez, J.; Yao, W.; Xiao, D.; Zhu, X.Y.; May, A.F.; et al. Two-dimensional itinerant ferromagnetism in atomically thin Fe_3GeTe_2. *Nat. Mater.* **2018**, *17*, 778–782. [CrossRef] [PubMed]
146. Jin, C.H.; Tao, Z.; Kang, K.F.; Watanabe, K.; Taniguchi, T.; Mak, K.F.; Shan, J. Imaging and control of critical fluctuations in two-dimensional magnets. *Nat. Mater.* **2020**, *19*, 1290–1294. [CrossRef]
147. Jiang, S.W.; Shan, J.; Mak, K.F. Electric-field switching of two-dimensional van der Waals magnets. *Nat. Mater.* **2018**, *17*, 406–410. [CrossRef] [PubMed]
148. Huang, B.; Clark, G.; Klein, D.R.; MacNeill, D.; Navarro-Moratalla, E.; Seyler, K.L.; Wilson, N.; McGuire, M.A.; Cobden, D.H.; Xiao, D.; et al. Electrical control of 2D magnetism in bilayer CrI_3. *Nat. Nanotechnol.* **2018**, *13*, 544–548. [CrossRef]
149. Jiang, S.W.; Li, L.Z.; Wang, Z.F.; Mak, K.F.; Jie Shan, J. Controlling magnetism in 2D CrI_3 by electrostatic doping. *Nat. Nanotechnol.* **2018**, *13*, 549–553. [CrossRef]
150. Ding, B.; Li, Z.F.; Xu, G.Z.; Li, H.; Hou, Z.P.; Liu, E.K.; Xi, X.K.; Xu, F.; Yao, Y.; Wang, W.H. Observation of magnetic skyrmion bubbles in a van der Waals ferromagnet Fe_3GeTe_2. *Nano Lett.* **2020**, *20*, 868–873. [CrossRef]
151. Park, T.E.; Peng, L.C.; Liang, J.H.; Hallal, A.; Yasin, F.S.; Zhang, X.C.; Song, K.M.; Kim, S.J.; Kim, K.; Weigand, M.; et al. Neel-type skyrmions and their current-induced motion in van der Waals ferromagnet-based heterostructures. *Phys. Rev. B* **2021**, *104410*, 024427. [CrossRef]
152. Wang, H.; Wang, C.X.; Li, Z.A.; Tian, H.F.; Shi, Y.G.; Yang, H.X.; Li, J.Q. Characteristics and temperature-field-thickness evolutions of magnetic domain structures in van der Waals magnet Fe_3GeTe_2 nanolayers. *Appl. Phys. Lett.* **2020**, *116*, 192403. [CrossRef]
153. Chen, W.J.; Sun, Z.Y.; Wang, Z.J.; Gu, L.H.; Xu, X.D.; Wu, S.W.; Gao, C.L. Direct observation of van der Waals stacking–dependent interlayer magnetism. *Science* **2019**, *366*, 983–987. [CrossRef] [PubMed]
154. Schmid, I.; Marioni, M.A.; Kappenberger, P.; Romer, S.; Parlinska-Wojtan, M.; Hug, H.J.; Hellwig, O.; Carey, M.J.; Fullerton, E.E. Exchange bias and domain evolution at 10 nm scales. *Phys. Rev. Lett.* **2010**, *105*, 197201. [CrossRef]
155. Kirtley, J.R.; Paulius, L.; Rosenberg, A.J.; Palmstrom, J.C.; Holland, C.M.; Spanton, E.M.; Schiessl, D.; Jermain, C.L.; Gibbons, J.; Fung, Y.K.K.; et al. Scanning SQUID susceptometers with sub-micron spatial resolution. *Rev. Sci. Instrum.* **2016**, *87*, 093702. [CrossRef] [PubMed]
156. Finkler, A.; Vasyukov, D.; Segev, Y.; Ne'eman, L.; Lachman, E.O.; Rappaport, M.L.; Myasoedov, Y.; Zeldov, E.; Huber, M.E. Scanning superconducting quantum interference device on a tip for magnetic imaging of nanoscale phenomena. *Rev. Sci. Instrum.* **2012**, *83*, 073702. [CrossRef]
157. Vasyukov, D.; Anahory, Y.; Embon, L.; Halbertal, D.; Cuppens, J.; Neeman, L.; Finkler, A.; Segev, Y.; Myasoedov, Y.; Rappaport, L.; et al. A scanning superconducting quantum interference device with single electron spin sensitivity. *Nat. Nanotechnol.* **2013**, *8*, 639–644. [CrossRef]
158. Bagani, K.; Sarkar, J.; Uri, A.; Rappaport, M.L.; Huber, M.E.; Zeldov, E.; Myasoedov, Y. Sputtered $Mo_{66}Re_{34}$ squid-on-tip for high-field magnetic and thermal nanoimaging. *Phys. Rev. Appl.* **2019**, *12*, 044062. [CrossRef]
159. Ren, H.T.; Zhong, J.; Xiang, G. The progress on magnetic material thin films prepared using polymer-assisted deposition. *Molecules* **2023**, *28*, 5004. [CrossRef]
160. Chang, K.; Eichler, A.; Rhensius, J.; Lorenzelli, L.; Degen, C.L. Nanoscale imaging of current density with a single-spin magnetometer. *Nano Lett.* **2017**, *17*, 2367–2373. [CrossRef]
161. Balasubramanian, G.; Chan, I.Y.; Kolesov, R.; Al-Hmoud, M.; Tisler, J.; Shin, C.; Kim, C.; Wojcik, A.; Hemmer, P.R.; Krueger, A.; et al. Nanoscale imaging magnetometry with diamond spins under ambient conditions. *Nature* **2008**, *455*, 648–651. [CrossRef] [PubMed]
162. Ariyaratne, A.; Bluvstein, D.; Myers, B.A.; Bleszynski Jayich, A.C. Nanoscale electrical conductivity imaging using a nitrogen-vacancy center in diamond. *Nat. Commun.* **2019**, *9*, 2406. [CrossRef] [PubMed]
163. Vool, U.; Hamo, A.; Varnavides, G.; Wang, Y.; Zhou, T.X.; Kumar, N.; Dovzhenko, Y.; Qiu, Z.; Garcia, C.A.C.; Pierce, A.T. Imaging phonon-mediated hydrodynamic flow in WTe_2. *Nat. Phys.* **2021**, *17*, 1216–1220. [CrossRef]
164. Wörnle, M.S.; Welter, P.; Giraldo, M.; Lottermoser, T.; Fiebig, M.; Gambardella, P.; Degen, C.L. Coexistence of Bloch and N'eel walls in a collinear antiferromagnet. *Phys. Rev. B* **2021**, *103*, 094426. [CrossRef]

Disclaimer/Publisher's Note: The statements, opinions and data contained in all publications are solely those of the individual author(s) and contributor(s) and not of MDPI and/or the editor(s). MDPI and/or the editor(s) disclaim responsibility for any injury to people or property resulting from any ideas, methods, instructions or products referred to in the content.